

International Journal of Physical Sciences

Volume 10 Number 16 30 August, 2015

ISSN 1992-1950



*Academic
Journals*

ABOUT IJPS

The **International Journal of Physical Sciences (IJPS)** is published weekly (one volume per year) by Academic Journals.

International Journal of Physical Sciences (IJPS) is an open access journal that publishes high-quality solicited and unsolicited articles, in English, in all Physics and chemistry including artificial intelligence, neural processing, nuclear and particle physics, geophysics, physics in medicine and biology, plasma physics, semiconductor science and technology, wireless and optical communications, materials science, energy and fuels, environmental science and technology, combinatorial chemistry, natural products, molecular therapeutics, geochemistry, cement and concrete research, metallurgy, crystallography and computer-aided materials design. All articles published in IJPS are peer-reviewed.

Contact Us

Editorial Office: ijps@academicjournals.org

Help Desk: helpdesk@academicjournals.org

Website: <http://www.academicjournals.org/journal/IJPS>

Submit manuscript online <http://ms.academicjournals.me/>

Editors

Prof. Sanjay Misra

*Department of Computer Engineering, School of Information and Communication Technology
Federal University of Technology, Minna,
Nigeria.*

Prof. Songjun Li

*School of Materials Science and Engineering,
Jiangsu University,
Zhenjiang,
China*

Dr. G. Suresh Kumar

*Senior Scientist and Head Biophysical Chemistry
Division Indian Institute of Chemical Biology
(IICB)(CSIR, Govt. of India),
Kolkata 700 032,
INDIA.*

Dr. Remi Adewumi Oluyinka

*Senior Lecturer,
School of Computer Science
Westville Campus
University of KwaZulu-Natal
Private Bag X54001
Durban 4000
South Africa.*

Prof. Hyo Choi

*Graduate School
Gangneung-Wonju National University
Gangneung,
Gangwondo 210-702, Korea*

Prof. Kui Yu Zhang

*Laboratoire de Microscopies et d'Etude de
Nanostructures (LMEN)
Département de Physique, Université de Reims,
B.P. 1039. 51687,
Reims cedex,
France.*

Prof. R. Vittal

*Research Professor,
Department of Chemistry and Molecular
Engineering
Korea University, Seoul 136-701,
Korea.*

Prof Mohamed Bououdina

*Director of the Nanotechnology Centre
University of Bahrain
PO Box 32038,
Kingdom of Bahrain*

Prof. Geoffrey Mitchell

*School of Mathematics,
Meteorology and Physics
Centre for Advanced Microscopy
University of Reading Whiteknights,
Reading RG6 6AF
United Kingdom.*

Prof. Xiao-Li Yang

*School of Civil Engineering,
Central South University,
Hunan 410075,
China*

Dr. Sushil Kumar

*Geophysics Group,
Wadia Institute of Himalayan Geology,
P.B. No. 74 Dehra Dun - 248001(UC)
India.*

Prof. Suleyman KORKUT

*Duzce University
Faculty of Forestry
Department of Forest Industrial Engineering
Beciyorukler Campus 81620
Duzce-Turkey*

Prof. Nazmul Islam

*Department of Basic Sciences &
Humanities/Chemistry,
Techno Global-Balurghat, Mangalpur, Near District
Jail P.O: Beltalpark, P.S: Balurghat, Dist.: South
Dinajpur,
Pin: 733103,India.*

Prof. Dr. Ismail Musirin

*Centre for Electrical Power Engineering Studies
(CEPES), Faculty of Electrical Engineering, Universiti
Teknologi Mara,
40450 Shah Alam,
Selangor, Malaysia*

Prof. Mohamed A. Amr

*Nuclear Physic Department, Atomic Energy Authority
Cairo 13759,
Egypt.*

Dr. Armin Shams

*Artificial Intelligence Group,
Computer Science Department,
The University of Manchester.*

Editorial Board

Prof. Salah M. El-Sayed

*Mathematics. Department of Scientific Computing,
Faculty of Computers and Informatics,
Benha University. Benha ,
Egypt.*

Dr. Rowdra Ghatak

*Associate Professor
Electronics and Communication Engineering Dept.,
National Institute of Technology Durgapur
Durgapur West Bengal*

Prof. Fong-Gong Wu

*College of Planning and Design, National Cheng Kung
University
Taiwan*

Dr. Abha Mishra.

*Senior Research Specialist & Affiliated Faculty.
Thailand*

Dr. Madad Khan

*Head
Department of Mathematics
COMSATS University of Science and Technology
Abbottabad, Pakistan*

Prof. Yuan-Shyi Peter Chiu

*Department of Industrial Engineering & Management
Chaoyang University of Technology
Taichung, Taiwan*

Dr. M. R. Pahlavani,

*Head, Department of Nuclear physics,
Mazandaran University,
Babolsar-Iran*

Dr. Subir Das,

*Department of Applied Mathematics,
Institute of Technology, Banaras Hindu University,
Varanasi*

Dr. Anna Oleksy

*Department of Chemistry
University of Gothenburg
Gothenburg,
Sweden*

Prof. Gin-Rong Liu,

*Center for Space and Remote Sensing Research
National Central University, Chung-Li,
Taiwan 32001*

Prof. Mohammed H. T. Qari

*Department of Structural geology and remote sensing
Faculty of Earth Sciences
King Abdulaziz UniversityJeddah,
Saudi Arabia*

Dr. Jyhwen Wang,

*Department of Engineering Technology and Industrial
Distribution
Department of Mechanical Engineering
Texas A&M University
College Station,*

Prof. N. V. Sastry

*Department of Chemistry
Sardar Patel University
Vallabh Vidyanagar
Gujarat, India*

Dr. Edilson FERNEDA

*Graduate Program on Knowledge Management and IT,
Catholic University of Brasilia,
Brazil*

Dr. F. H. Chang

*Department of Leisure, Recreation and Tourism
Management,
Tzu Hui Institute of Technology, Pingtung 926,
Taiwan (R.O.C.)*

Prof. Annapurna P.Patil,

*Department of Computer Science and Engineering,
M.S. Ramaiah Institute of Technology, Bangalore-54,
India.*

Dr. Ricardo Martinho

*Department of Informatics Engineering, School of
Technology and Management, Polytechnic Institute of
Leiria, Rua General Norton de Matos, Apartado 4133, 2411-
901 Leiria,
Portugal.*

Dr Driss Miloud

*University of mascara / Algeria
Laboratory of Sciences and Technology of Water
Faculty of Sciences and the Technology
Department of Science and Technology
Algeria*

Prof. Bidyut Saha,

*Chemistry Department, Burdwan University, WB,
India*

ARTICLES

- Performance enhancement of incoherent spectral amplitude encoding-optical code division multiple access (SAE-OCDMA) by using dispersion compensation fiber Bragg grating (FBG)** 466
Ibrahim Luay Abdul Jabbar and Tahreer Safa Mansour
- Geophysical assessment of potential hydrological units in hydrologically challenged geomaterials of Makurdi, Benue State, Nigeria** 479
Daniel N. Obiora, Johnson C. Ibuot and Nyakno J. George
- Effect of tempering on the microstructure and mechanical properties of austenitic dual phase steel** 490
Sunday Chukwuyem IKPESENI, Obimma Basil ONYEKPE and Monday Itopa MOMOH
- Existence of solution for a third order three point boundary value problem at resonance** 498
S. A. Iyase and M. C. Agarana

Full Length Research Paper

Performance enhancement of incoherent spectral amplitude encoding-optical code division multiple access (SAE-OCDMA) by using dispersion compensation fiber Bragg grating (FBG)

Ibrahim Luay Abdul Jabbar* and Tahreer Safa Mansour

Institute of Laser for Postgraduate Studies, Baghdad University, Baghdad, Iraq.

Received 3 June, 2015; Accepted 13 July, 2015

Incoherent spectral amplitude encoding optical code division multiple access (SAE-OCDMA) based on fiber Bragg grating (FBG) is one promising technique aim to improve local area networks to have longer span telecommunication network type. In this study, the performance enhancement incoherent SAE-OCDMA is achieved when a dispersion compensation fiber Bragg grating (DCFBG) and erbium doped fiber amplifier (EDFA) are used in optical link. Though, the results can be obtained, these components give good indicator on system performance. In the design, DCFBG is introduced as the dispersion compensation to eliminate the effect of the positive dispersion. This leads to reduce multiple access interference (MAI). While EDFA, is used to compensate loss in conventional single mode fiber (SMF). As a result, the maximum bit error rate (BER) reaches 10^{-9} and 10^{-6} for 3 and 7 users, respectively without DCFBG and EDFA at 40 km, respectively, but with DCFBG, the maximum BER reaches 10^{-21} and 10^{-10} for 3 and 7 Users, respectively, at the same distance. In this presence case, EDFA and DCFBG are together in optical channel, the maximum BER reaches 10^{-22} and 10^{-12} for 3 and 7 users respectively at the same distance (40 km). So that, the transmission distance is improved to 160 and 140 km for 3 and 7 Users, respectively. Simulation results presented in this study are obtained using Opti system and Opti Grating Softwares.

Key words: Spectral amplitude encoding-optical code division multiple access (SAE-OCDMA), dispersion compensation fiber Bragg grating (DCFBG), multiple access interference (MAI), phase induced intensity noise (PIIN), Walsh hadamard code (WH code).

INTRODUCTION

Recently, interest has increased in spectral-amplitude-encoding optical code-division multiple access (SAE-OCDMA) systems based on fiber Bragg grating due to

their ability to assuage multiple access interference (MAI) influence on performance, in addition to their cost savings (Shastri et al., 2008; Al-Khafaji et al., 2012). Where

*Corresponding author. E-mail: ibrahimluay123@gmail.com

Author(s) agree that this article remain permanently open access under the terms of the [Creative Commons Attribution License 4.0 International License](https://creativecommons.org/licenses/by/4.0/)

Spectral Amplitude encoding (SAE) technique was first demonstrated by Zaccarin and Kavehrad (1995). SAE-OCDMA is one of the competing technologies for future multiple access networks, and it achieved multiplexing transmission and multiple accesses by coding in the optical domain, which supports multiple subscribers in the same time slot and the same frequency (Yin and Richardson, 2007).

SAE-OCDMA systems design is based on encoding the information signal in the time domain by a pseudorandom sequence. Efficient systems for use in local area network (LAN) environments can be obtained. It will always suffer from a basic limitation. As the number of simultaneous active users is increased, the code length has to be increased in order to maintain the same performance. In such systems, that will refer to as SAE-OCDMA systems, the coding is done in the wavelength domain while in the usual CDMA systems, the code multiplies the modulation signal in the time domain (Kavehrad, 1995). To improve the bit error rate of the system multi-fiber, Bragg gratings are used at transmitter and receiver ends with same reflectivity (Ranjan, 2014).

A fiber Bragg grating (FBG) is a type of distributed Bragg reflector constructed in a short segment of optical fiber that reflects particular wavelengths of light and transmits all others. Reflectivities approaching 100% are possible, with the grating bandwidth tailored from typically 0.1 nm to more than tens of nanometers. These characteristics make Bragg gratings suitable for telecommunications, where they are used to reflect, filter or disperse light (Hill et al., 1978). The FBG written by ultraviolet light (UV) into the core of an optical fiber has developed into a critical component for many applications in fiber-optic communication and sensor systems. When ultraviolet light radiates an optical fiber, the refractive index of the fiber is changed permanently; the effect is termed photosensitivity. The change in refractive index is permanent in the sense that it will last for decades (life times of 25 years are predicted) if the optical waveguide after exposure is annealed appropriately, that is by heating for a few hours at a temperature of 50°C above its maximum operating temperature (Erdogan et al., 1994).

Practically, the most commonly used light sources are KrF, ArF excimer lasers and femtosecond laser that generate 248, 193 and 264 nm, respectively, optical pulses (pulse width 10 ns and 260 fs) at pulse repetition rates of 50 to 75 pulses/s and 1- 500 KHZ, respectively. The typical irradiation conditions are an exposure to the laser light for a few minutes at intensities ranging from 100 to 1000 mJ/cm². Under these conditions, Δn is positive in germanium doped fiber with a magnitude ranging between 10⁻⁵ for weak grating to 10⁻³ for strong grating (Erdogan et al., 1994).

Advantages of fiber Bragg gratings over competing technologies include all-fiber geometry, low insertion loss,

high return loss or extinction, and potentially low cost. But the most distinguishing feature of fiber gratings is the flexibility they offer for achieving desired spectral characteristics. Multi-physical parameters can be changed, including: induced index change, length, apodization, period chirp, fringe tilt, and whether the grating supports counter-propagating or co-propagating coupling at a desired wavelength (Erdogan et al., 1994). Multi-fiber Bragg gratings (FBGs), having the same bandwidth and different Bragg wavelengths are used to obtain the signature codes in SAE-OCDMA (Tiwari and Singh, 2013). OCDMA supports multiple asynchronous, concurrent users which occupy the same time slots and frequency domain. In addition, OCDMA systems have the advantages of providing multiple users to simultaneously access the same bandwidth with high-level security (Aljunid et al., 2004).

Nonetheless, the OCDMA systems suffer from different noises such as a shot noise, thermal noise, a dark current and a phase-induced intensity noise (PIIN). In addition, multiple access interference (MAI) associated with availability of many users is considered as a dominating system-degradation factor for the OCDMA networks. Therefore, intelligent design of the code sequence is important when reducing contribution of the MAI to the total optical power received (Stok and Sargent, 2000).

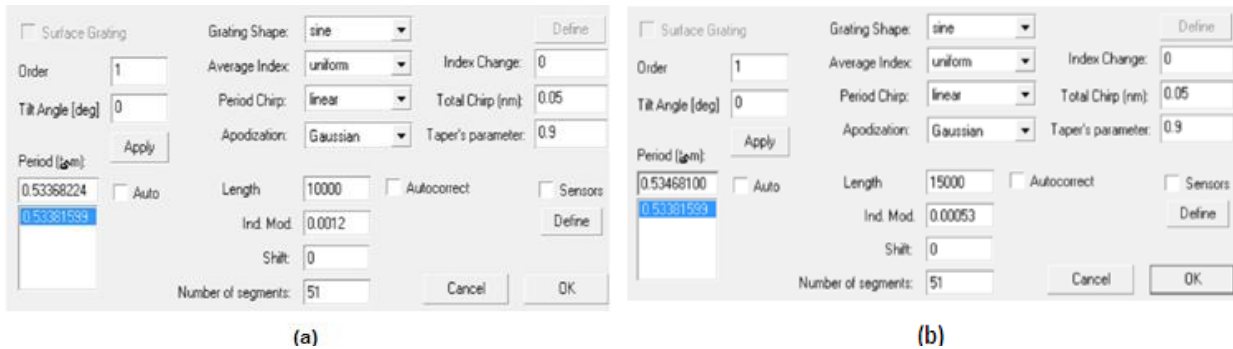
Accordingly, SAE-OCDMA technologies have been introduced, to result in good solutions which have reduced the effect of MAI by utilizing codes with fixed in-phase cross-correlation (Noshad and Jamshidi, 2010). In addition, the balance scheme shows that MAI can be eliminated with Hadamard code (Smith et al., 1998). To support a high-capacity (SAE-OCDMA) transmission, the embedded standard fiber Bragg grating (FBG) should be up rated to overcome the dispersion limit. Dispersion compensating fibers (DCF) have been extremely used to compensate the positive dispersion to improve transmission distance (Raad et al., 2012). But the insertion of DCF increases the aggregate loss, cost of the optical transmission system and nonlinear effects. In addition, the magnitude of compensation is wavelength dependent and can only be quite achieved in a relatively narrow band (Agrawal, 1997). Therefore, dispersion compensation fiber Bragg grating (DCFBG) has also been proposed recently for positive dispersion compensation and is known as a perfect alternative to DCF.

The aim of this study is to obtain the best performance of SAE-OCDMA by using dispersion compensation fiber Bragg grating, multi-FBG and optical amplifier.

MATERIALS AND METHODS

Description of spectral amplitude

With development and ripeness of FBGs, they can be employed as the choosing wavelength filters to implement the Spectral Amplitude



Profile 1. Structure parameters of Array-FBG a- 3 Users b- 7 Users.

Table 1. Bragg wavelengths for 3 user.

Period grating (nm)	Bragg wavelengths (nm)
534.5088001	1552
533.9577601	1550.4
533.6822400	1549.6
533.1312001	1548

Encoding (SAE). The implementation of SAE-OCDMA is to overcome the deficiency of the bulk-optic spectral amplitude encoder/decoder. The spectral amplitude operates where the light pulse from an incoherent light source is modulated by data, and also go through the FBGs with different wavelength to determine the chosen user's address code word (Shalaby et al., 2001). SAE was introduced to eliminate the MAI existing in conventional OCDMA systems.

SAE systems use complementary detection technique to recover the original signals (Smith et al., 1998). The effect of MAI can be eliminated by using subtraction detection technique. The most common subtraction detection technique is the complementary subtraction detection technique, which is also known as balanced detection technique (Kavehrad, 1995). This balance receiver is used as a part of receiver which filters the incoming signals. For unmatched transmitters, half of transmitter spectral components will match the direct filter and the other half will match the complementary filter. The output of the balance receiver represents the difference between the two parts, with unmatched channels being cancelled. It is possible to design codes with the full orthogonality in the incoherent spectral intensity OCDMA system, since there is a subtraction between two photo detectors. In this system, the signature sequence is spread across different wavelength with each chip occupying different wavelength. The advantage of optical spreading CDMA is that; it does not need synchronization as the chip spreads in frequency and not in time (Kavehrad, 1995). Incoherent SAE-OCDMA is a good candidate for optical multiple access networks over other OCDMA techniques. The incoherent source appears as a good indicator for SAE as it is inherently broadband, a necessary characteristic of SAE (Fadhil et al., 2010). The important feature of the SAE-OCDMA systems is that multiple access interference (MAI) can be eliminated by code sequences of a fixed in-phase cross-correlation value. This study uses Walsh-Hadamard codes as signature codes (S-Pin, 2003).

Building of multi-FBG as encoder/decoder

The characteristics response from Bragg Grating can be analyzed as fully described by:

1. The center wavelength of grating λ_B .
2. Peak reflectivity Rmax of grating which occur at λ_B .
3. Physical length of grating L .

Thus, the designed multi -FBG parameters structure can be summarized in Profile 1 for 3 and 7 users.

Thus, parameters set of multi-FBG are shown in Tables 1 and 2 for 3 and 7 users, respectively, depending on the center wavelength of grating which can be expressed as this in Equation 1.

$$\lambda_B = 2.n_{eff} .\Lambda \tag{1}$$

Where :- n_{eff} : is the effective refractive index of the fiber core; Λ : is the period of FBG.

After setting, these Bragg wavelengths used to implement the SAE in OCDMA (Table 3) show some parameters that are related to multi -FBG for 3 and 7 users by using OptiGrating Software. Thus, the grating spectrum of multi-FBG for 3 and 7 users, respectively can be shown with opti Grating software (Figure 1a to b).

Dispersion compensation FBG

Chromatic dispersion compensation using highly efficient reflective FBGs is fundamentally different from the incumbent technology used for dispersion compensation, namely Dispersion Compensation Fiber (DCF).

Table 2. Bragg wavelengths for 7 user.

Period grating (nm)	Bragg wavelengths (nm)
534.6810001	1552.5
534.5088001	1552
534.3366001	1551.5
534.1644001	1551
533.9922001	1550.5
533.8200001	1550
533.6478001	1549.5
533.4756001	1549

Table 3. Show, peak reflectivity, FWHM, and effective refractive index.

Parameter	3 users	7 users
Reflectivity	0.9999999	0.99994
FWHM	0.6	0.3
n_{eff}	1.451800232	1.451800232

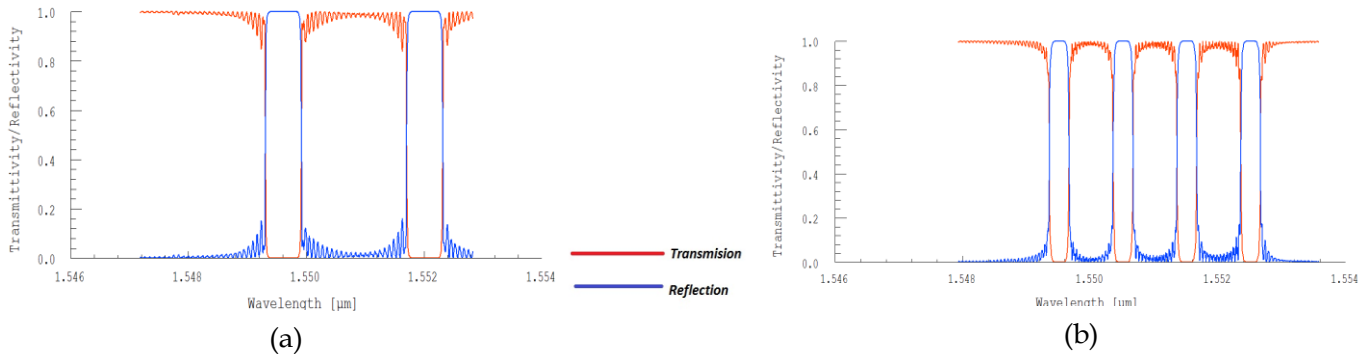


Figure 1a-b. Grating spectrum of multi-FBG a-3 users b-7 users.

After 40 km propagation in SMF, the accumulated dispersion is 670 ps/nm. In order to compensate for this accumulated dispersion, the corresponding option Dispersion in the main tab of the Ideal Dispersion Compensation FBG is fixed as -670 ps/nm Equation (2).

$$D_T = D_{SMF} \times L_{SMF} \tag{2}$$

Where: D_T : is the accumulated dispersion in optical link; D_{SMF} : is the dispersion of SMF, typically is 16.75 ps/nm-km; L_{SMF} : is the length of optical fiber.

The bandwidth of DCFBG (B_{DCFBG}) used in the simulation calculated from.

$$B_{DCFBG} = \Delta\lambda \tag{3}$$

Where: $\Delta\lambda$: is the line width of incoherent optical source.

Thus, the line width of incoherent optical source can be expressed by Equation 4 (S-Pin Tseng, 2003).

$$\Delta\lambda = \Delta f / (c / \lambda^2) \tag{4}$$

$$\Delta f = P_{average} / PSD \tag{5}$$

Where: $P_{average}$: is the average power of incoherent optical source.

It can be measured with power meter; PSD : is the average value of the power spectral density of incoherent optical source that can be calculated in Equation 5 (Raad et al., 2012); Δf : is the linewidth of optical source in frequency; λ : is the wavelength of incoherent optical source; c : is the speed of light in Vacuum.

Finally, how to use an ideal dispersion component in optisystem software for dispersion compensation in SAE-OCDMA is explain.

Table 4. Walsh Hadamard code with length of 4 for 3 user.

Walsh Hadamard codes	Wavelengths
1010	FBG1-FBG3
1100	FBG2-FBG3
1001	FBG1-FBG2

Table 5. Walsh Hadamard code with length of 8 for 7 user.

Walsh Hadamard codes	Wavelengths
10101010	FBG1-FBG3- FBG5-FBG7
11001100	FBG2-FBG3- FBG6-FBG7
10011001	FBG1-FBG2- FBG5-FBG6
11110000	FBG4-FBG5- FBG6-FBG7
10100101	FBG1-FBG3- FBG4-FBG6
11000011	FBG2-FBG3- FBG4-FBG5
10010110	FBG1-FBG2- FBG4-FBG7

Code construction and properties

Walsh-Hadamard consists of the row vector of a Walsh code matrix is arranged according to the order of Hadamard. It is also called Walsh code (Yen et al., 2013). The elements of this Walsh matrix are ± 1 , which can be rapidly generated from the following recursion relation:

$$A(i+1) = \begin{bmatrix} +A(i) + A(i) \\ +A(i) - A(i) \end{bmatrix} \quad (6)$$

For 3 users SAE-OCDMA network, the code word of $A(2)$ is used. Why, for 7 users SAE-OCDMA network, the code word of $A(3)$ is used. $A(2)$ is a 4×4 Walsh matrix; while $A(3)$ is a 8×8 Walsh Matrix. But the 1st line of the code from both matrixes is consisting of a group of logic "1". The row of logic "1" is not in use, as though the decoding processing, the data will be extracted out by using multi-FBGs (Tables 4 and 5).

Incoherent SAE-OCDMA system model

In OCDMA System, SAE is most effective because of assigning unique code to each user. SAE technique which is operated on bit rate is a cost effective technique for end users. SAE-OCDMA systems use cheap incoherent white Light sources for SAE, but also affected by Phase Induced Intensity Noise (PIIN). PIIN noise largely limits the performance of SAE-OCDMA systems. PIIN arises due to the incoherent light mixing and incident on a photo-detector, less cross-correlation values between signature codes, and reduces the MAI and PIIN effectively; hence increase the SAE-OCDMA system performance. In addition, dispersion in SMF-28(GVD) is also an important system limitation for long transmission distance which must be reduced. Thus, DCFBG is reducing the effect of dispersion in network.

The adopted block diagram of incoherent SAE-OCDMA for 3-users based on DCFBG is presented in Figure 2.

SAE-OCDMA for 3-users and 7 users

In this design, Incoherent White light source used in the transmitter

section and number of FBGs is specified with respect to the code weight. SAE uses Walsh-Hadamard code with weight 2 for 3 user and weight 4 for 7 user. The electric data of each user is modulated by Mach-Zehnder modulator (MZ) on a White light source to obtain intensity modulated signal. Then the modulated pulse goes through the multi-FBG with different wavelengths (as encoders and decoders for the incoherent optical signal). Finally, before transmitting signal by the optical channel, all users are collected by a Power combiner and transmitted through the channel. The receiver is comprised of a spectral filter and a photo detector connected in a balanced configuration which performs the decoding with a low-pass filter and a BER analyzer.

RESULTS AND DISCUSSION

The simulation parameters in Optisystem software are chosen for 3 and 7 users SAE-OCDMA as shown in Table 6. The Incoherent SAE-OCDMA for computing BER tester, eye diagram analyzer and quality factor values for different methods use BER analyzer.

Effect of the transmitted power on BER with and without DCFBG

Many parameters influence this system performance which are formerly available as transmitted power, the required input power at the receiver to obtain the desired bit error rate (BER), the overall system loss and bandwidth are shown in Figure 3a and b, the BER as a function of input power for 3 and 7 users respectively use DCFBG. When the average power of incoherent optical source is increased, BER is decreased, but when the input power reaches approximately 2 and 6 mW for 3 and 7 users, respectively, after that the BER value remain stable. Due to this, each of the system has optimum power, so that the

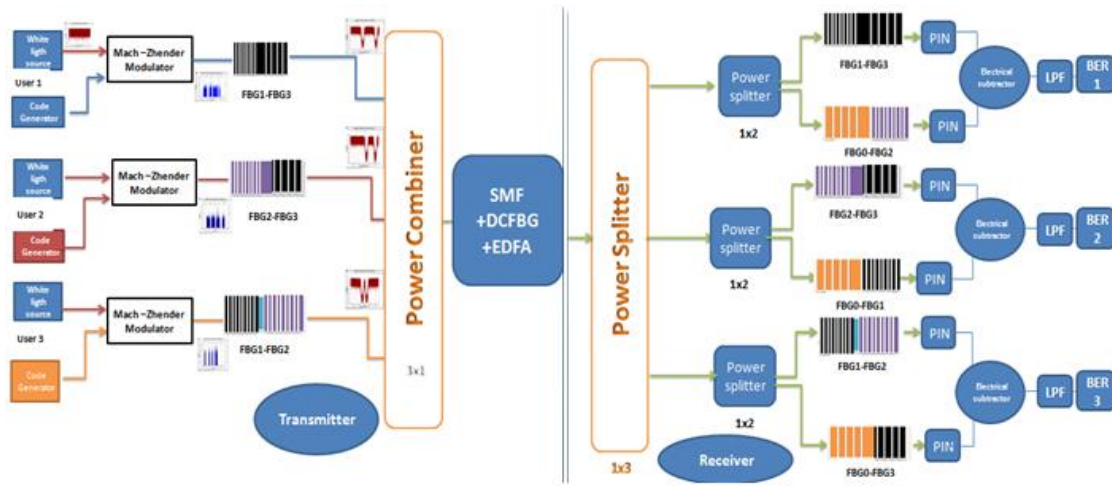


Figure 2. Block diagram of 3 user Incoherent SAE-OCDMA.

Table 6. Incoherent SAE-OCDMA simulation parameters.

Parameter	7 Users	3 Users
Operating wavelength	1550.75 nm	1550 nm
Power spectral density	9.6×10^{-15} W/Hz	3.2×10^{-15} W/Hz
Fiber length	40 km	40 km
Extinction ratio (MZ)	60 dB	60 dB
Fiber attenuation	0.2 dB/km	0.2 dB/km
Dark current	5 nA	5 nA
Responsivity	1 A/W	1 A/W
Receiver filter bandwidth	140 MHz	140 MHz
Erbium doped fiber amplifier (EDFA) Gain	20 dB	20 dB
Signal bit rate	200 Mbps	200 Mbps
Bit rate	10 Gchip/s	10G chip/s
Sequence length	1024 bit	1024 bit
Samples per bit	64 sample	64 sample

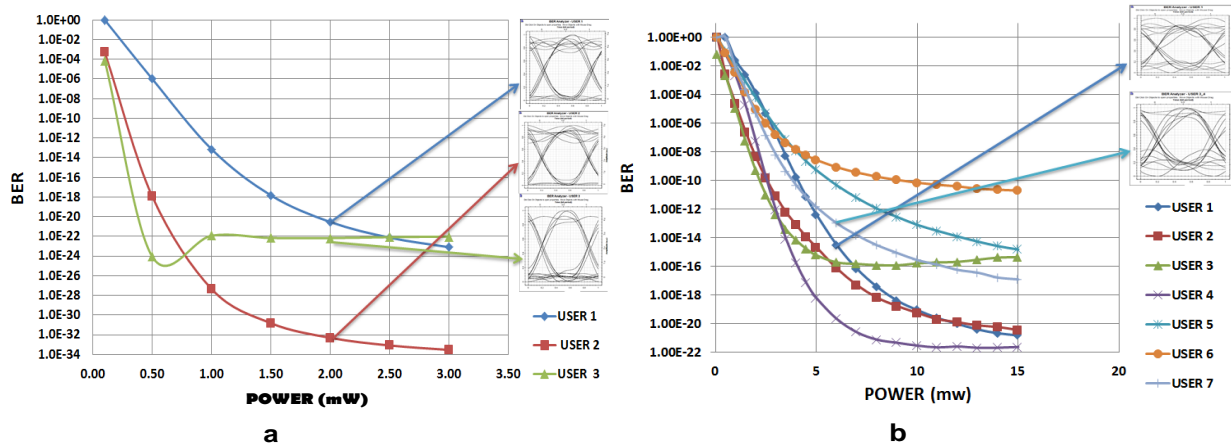


Figure 3. (a). Plotting of input power versus BER presence DCFBG for 3 Users. (b) Plotting of input power versus BER presence DCFBG for 7 Users.

Table 7. BER for 3 and 7 users at 40 km.

Users	3 User
	DCFGB is present
BER1	2.9×10^{-21}
BER2	4.9×10^{-33}
BER3	6.8×10^{-23}
Users	7 User
	DCFGB is present
BER1	3.35×10^{-15}
BER2	7.67×10^{-17}
BER3	1.95×10^{-16}
BER4	2.25×10^{-20}
BER5	4.78×10^{-11}
BER6	8.74×10^{-10}
BER7	1.07×10^{-13}

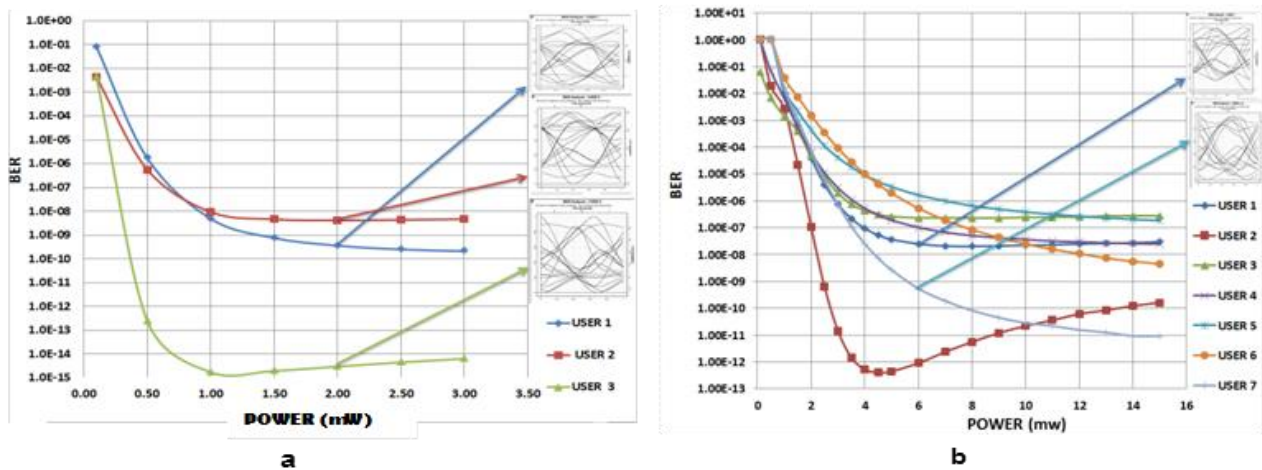


Figure 4. (a) Plotting of input power versa BER absence DCFBG for 3 Users. (b) Plotting of input power versa BER absence DCFBG for 7 Users.

optimum power for 3 and 7 users are 2 and 6 mW respectively in SAE-OCDMA. When the transmitted power increases until it reaches the optimal values, a signal to noise ratio (SNR) is increased, the BER leads is reduced. In addition, the BER value is reduced with the presence of DCFGB at 40 km optical link (Table 7). DCFGB allows the long wavelength (red wavelength) travels fast than the short wavelength (blue wavelength). This mechanism operates to reduce the pulse broadening, to prevent crosstalk between pulses. This process leads to enhance the signal power. Therefore, BER is improved.

When DCFBG is neglected, the BER reaches 3.6×10^{-10} , 4.18×10^{-9} , and 3.02×10^{-15} for User 1, 2 and 3, respectively, at 40 km as shown in Figure 4(a). The BER value is increased compared with the BER value (Figure

3a), due to a single mode fiber G-652 used between the transmission and receiver sides in SAE-OCDMA contains the material dispersion. The value of the material dispersion is increased, when the length of a SMF becomes bigger than 40 km. Thus, the transmitted power increases in this case, which does not affect the BER value, because of the effect of the material dispersion. The material dispersion cause the pulse broadening, so that, this effect appears on the BER value (Figure 4b).

The BER becomes large than 10^{-9} for 7 users. Due to this increase, a number of users can be affected on the performance of system although input power increased. In addition, the effect of material dispersion on the system performance, where BER value oscillate between ($10^{-6} \sim 10^{-13}$) at the same distance (40 km), where incoherent

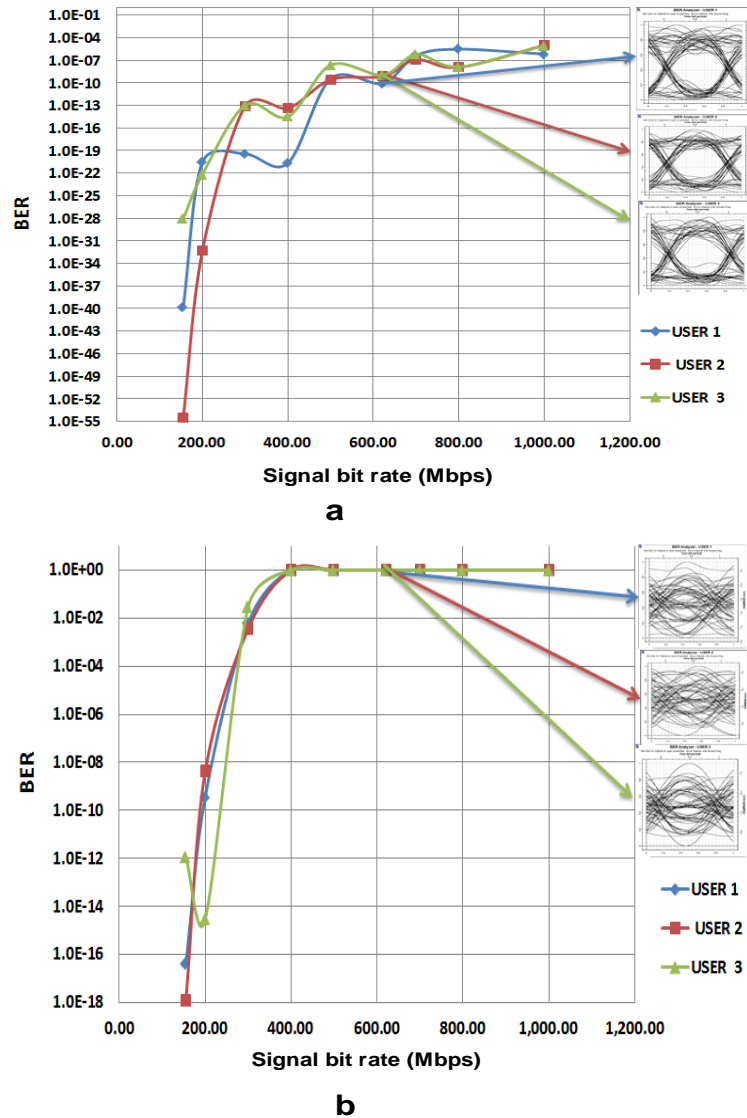


Figure 5. (a) Plotting of signal bit rate versa BER presence DCFBG for 3 Users. (b) Plotting of signal bit rate versa BER absence DCFBG for 3 Users.

SAE-OCDMA suffers from phase induced intensity noise, especially when the number of active users are increasing with low power. But an incoherent optical source prefers SAE-OCDMA because it is producing same power on the overall bandwidth of pulse. Therefore, DCFBG, MAI and PIIN are increased in this case, and Q-factor value and eye diagram opening are reduced.

Effect of signal bit rate on BER with and without DCFBG

Figure 5(a) shows the BER at the receiver side increased

with increasing signal bit rate, where BER becomes 9.2×10^{-9} , 7.3×10^{-10} and 1.12×10^{-9} for User 1, 2 and 3, respectively, at 40 km with 622 Mbps a presence DCFBG. While BER becomes large than 10^{-9} without DCFBG after 200 Mbps as shown in Figure 5(b). Due to, the effect of positive dispersion in SMF becomes more with a high signal bit rate. So, when a signal bit rate changes from 200 Mbps into 622 Mbps without DCFBG, in this case, the MAI effect is increased, therefore, the BER value is also increased. Thereby, a DCFBG plays important role to reduced the effect of a positive dispersion to reduce MAI effect when a signal bit rate was increased in an incoherent SAE-OCDMA for 3 user.

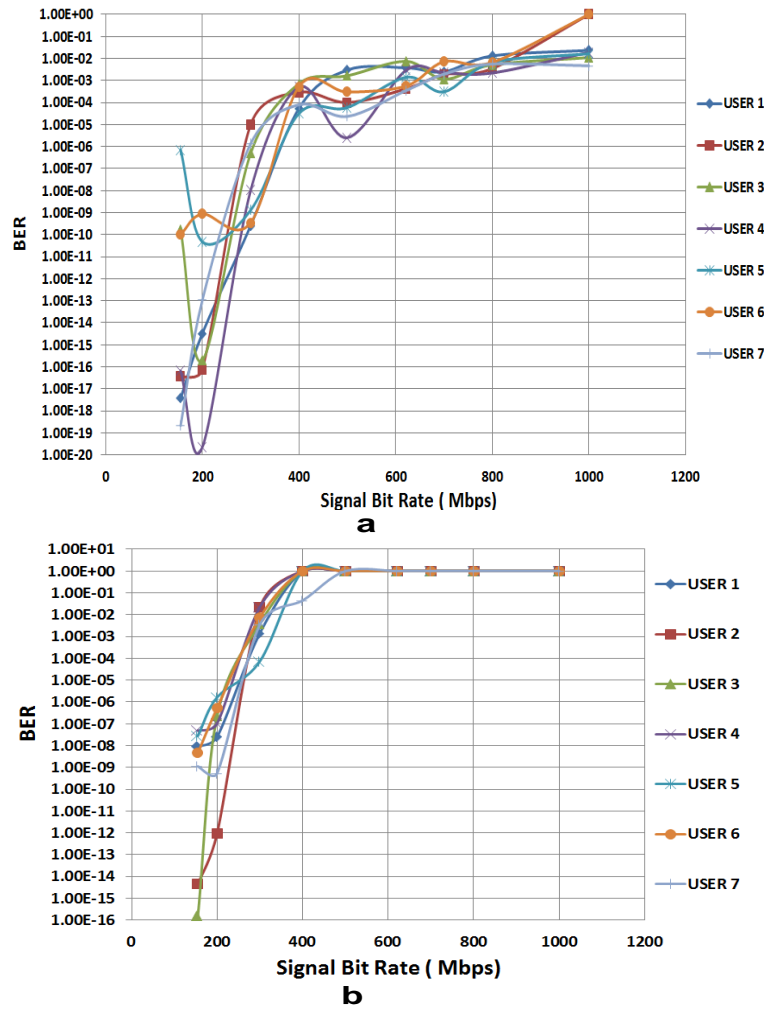


Figure 6. (a) Plotting of signal bit rate versa BER presence DCFBG for 7 Users. (b) Plotting of signal bit rate versa BER absence DCFBG for 7 Users.

In the case of the 7th user, the BER value appears larger than 10^{-9} , the presence or absence of DCFBG at 622 Mbps are shown in Figure 6 (a and b). With the number of simultaneous active users, data rate and the positive dispersion effect are increased, inter symbol interference is also increased, this leads the performance of system deteriorates. In addition, an incoherent optical source can be consider more suitable with the low data rate, not suitable with a high data rate. But, an incoherent white light source prefers to use SAE rather than the coherent optical source because, the coherent source is not able to transmit more user data, due to the line width of a coherent source is very narrow. In addition, the coherent source suffers from optical beat noise (OBN). So, a high data rate in an incoherent SAE-OCDMA for 7 users, aim to increase the MAI effect, an effect for the material dispersion will appear on the system

performance until, if the effect of material dispersion is little. Therefore, the BER values appears to be bad with DCFBG as show in Figure 6 (a), but, absence of DCFBG in the BER values appear to be very bad as show in Figure 6 (b).

Effect of fiber length on BER with and without DCFBG

Figures 7 and 8 display the variation of BER for each user with different fiber length in the absence and presence of dispersion compensation FBG. The BER can be explain with Table 8 for absence and presence of DCFBG at 50 km.

Note from results in Table 8, the BER improves with DCFBG. When the fiber length is increased, the

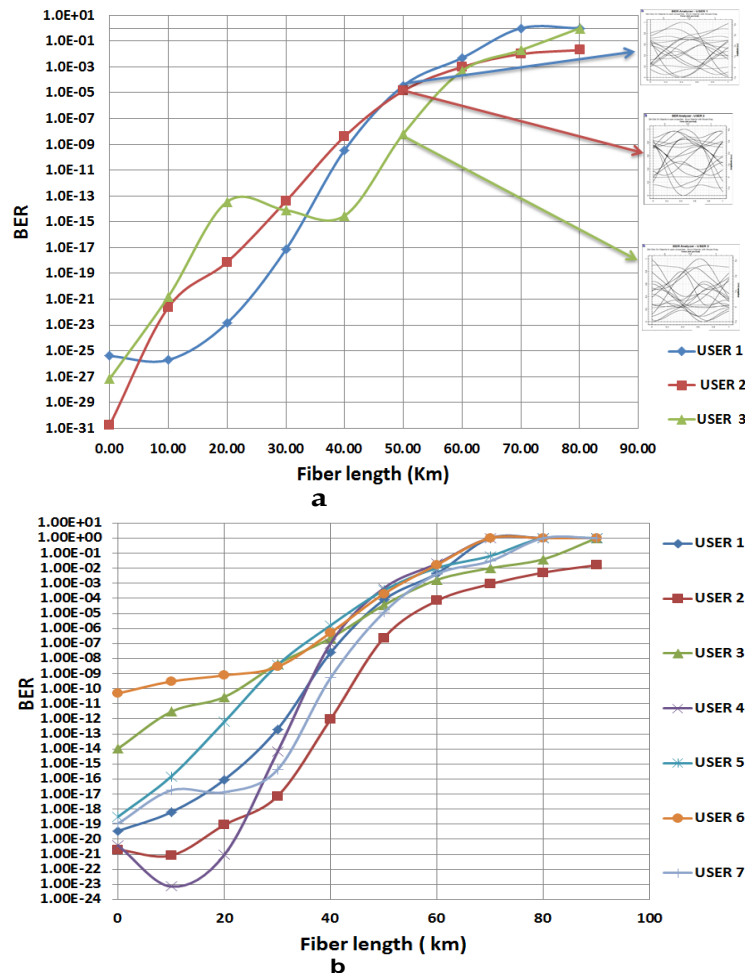


Figure 7. (a) Plotting of fiber length versus BER without DCFBG for 3 Users. (b) Plotting of fiber length versus BER without DCFBG for 7 Users.

dispersion of optical fiber will be increased to 16.75 ps/nm for each kilometer. This dispersion produced broadening pulses, thereby, a MAI appears. To prevent it, DCFBG solves these problems. Therefore, DCFBG improves transmission distance, thereby, to enhance local area network to longer span telecommunication network. Where the transmission distance may up to 40 km, 30 km for 3 and 7 users, respectively, in the case of absence of DCFBG, where the BER value at these distances are less than 10^{-9} are shown in Figure 7a and b. While it may up to 70 and 50 km for 3 and 7 users, respectively, the presence of DCFBG are shown in Figure 8 a and b. The BER value is also enhanced by using DCFBG.

Effect of fiber length on BER with DCFBG and EDFA

When DCFBG and EDFA both are used in optical link, the

BER value for each user becomes good value. From Figure 9(a), the BER value for user 1, 2 and 3 are 1.25×10^{-9} , 1.57×10^{-16} , and 1.619×10^{-12} , respectively at 160 km. There are two important factors affected on the system performance. The first factor is the attenuation in a SMF. Where the fiber attenuation are equal to 0.2dB/km. Another factor is the chromatic dispersion. The gain in the main tab of the erbium doped fiber amplifier (EDFA) is fixed as 20 dB. This value suffices to compensate a fiber losses, especially, when the fiber length is equal to 100 km. Thus, the gain in optical amplifier (EDFA) depend on a fiber attenuation for each kilometer and fiber length in this system. In addition, splice and connector losses. EDFA can be used to compensate a fiber loss in an optical channel, therefore, EDFA is very important in the large distance. Also, a DCFBG has recently had a lot of attention as a mean of increasing the transmission capacity and the transmission distance. Where the dispersion coefficient in SMF is

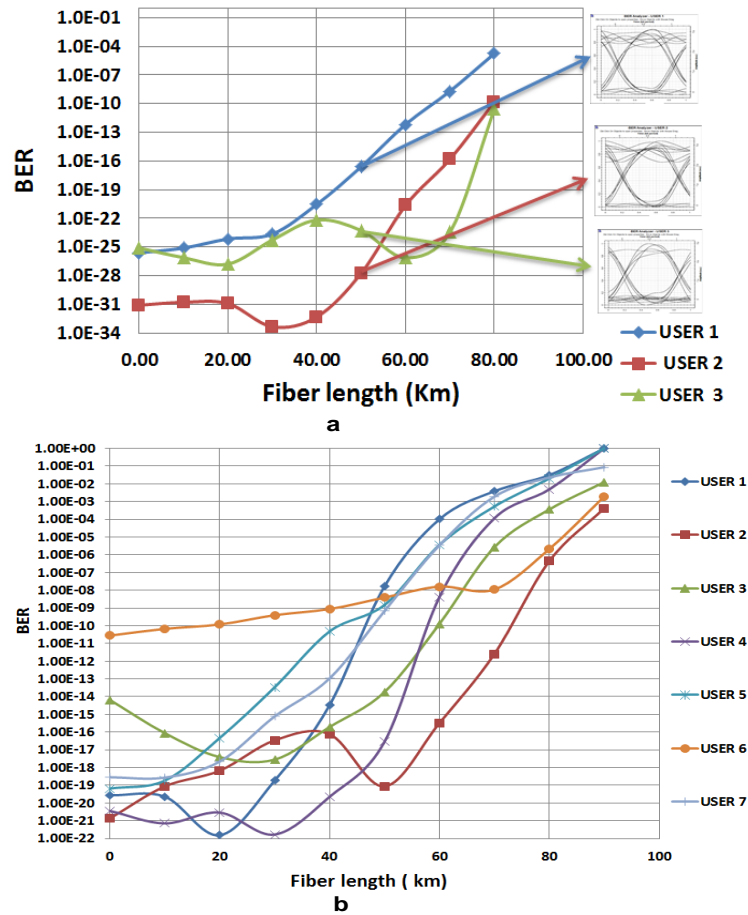


Figure 8. (a) Plotting of fiber length versus BER with DCFBG for 3 Users. (b) Plotting of fiber length versus BER with DCFBG for 7 Users.

Table 8. BERs for 3 and 7 users at 50 km.

Users	3 User	
	Without DCFBG	With DCFBG
BER1	3.55×10^{-5}	2.5×10^{-17}
BER2	1.40×10^{-5}	1.79×10^{-28}
BER3	6.6×10^{-9}	5.46×10^{-24}
Users	7 User	
	Without DCFBG	With DCFBG
BER1	8.02×10^{-5}	1.68×10^{-8}
BER2	2.4×10^{-7}	8.68×10^{-20}
BER3	3.58×10^{-5}	1.83×10^{-14}
BER4	4.74×10^{-4}	2.87×10^{-17}
BER5	3.38×10^{-4}	1.49×10^{-9}
BER6	2×10^{-4}	3.88×10^{-9}
BER7	1.16×10^{-5}	6.74×10^{-10}

16.75 ps/nm-km, and the fiber length is 100 km, the positive dispersion value becomes 1675 ps/nm. So, the

dispersion in the main tab of DCFBG is fixed as -1675ps/nm. This value suffices to compensate a positive

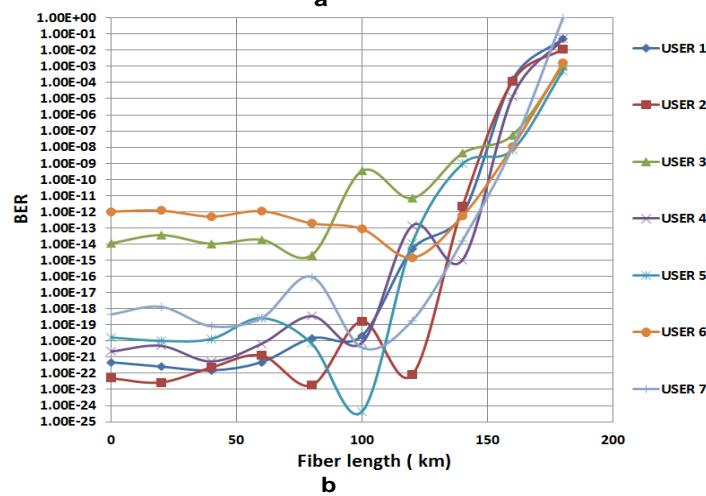
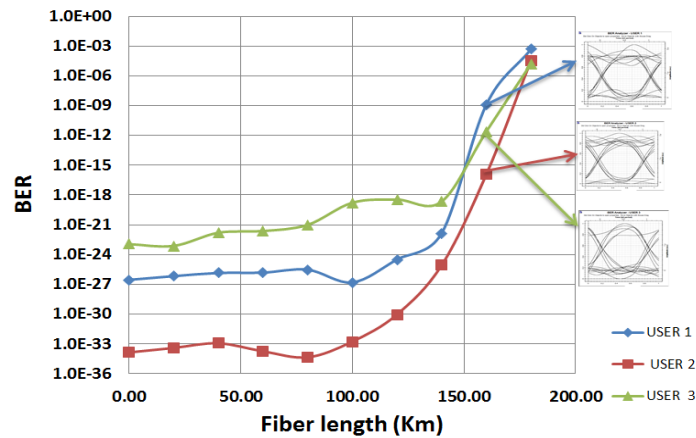


Figure 9. (a) Plotting of fiber length versa BER with DCFBG and EDFA for 3 Users. (b) Plotting of fiber length versa BER with DCFBG and EDFA for 7 Users.

Table 9. Explain Q-factor for 3 users at 160 km.

Q-factor	Absence EDFA+DCFBG	Presence EDFA+DCFBG
User 1	0.00	5.95
User 2	0.00	8.16
User 3	0.00	6.94

dispersion.

Therefore, an optical transmission distance improved to 160 km and 140 km for 3 and 7 user, respectively by using DCFBG and EDFA together. when the number of users increases to 7 users, the BER, presence EDFA and DCFBG together, can obtain less than 10^{-9} at 140 km as shown in Figure 9(b). Note, DCFBG and EDFA together are used to overcome losses in optical link such as attenuation and group velocity dispersion (GVD) to obtain

the best signal to noise ratio, eye opening and quality factor as shown in Table 9. Also, note from Figure 9(b), shows BER values for the most user become less at 100 km. Due to this, there is gain effect in EDFA. Also, note from all results can be explain in all figures, the BER value is different from one user to another. Due to non ideal FBG, there is an incoherent light source (amplified spontaneous emission) and a positive/a negative dispersion in SMF.

Conclusion

In this study, the performance enhancement of Incoherent SAE-OCDMA using dispersion compensation fiber Bragg grating and erbium doped fiber amplifier were studied. The proposed SAE-OCDMA system implemented using DCFBG were used to achieve low bit error rate, large transmission distance and large data capacity. These results are valuable for improving system performance by using DCFBG, where the BER is reduce twice by using DCFBG and EDFA together. As seen from results, Single mode fiber (SMF) with DCFBG and EDFA, improve the fiber length and BER compare with absence DCFBG. When the effects of dispersion and attenuation in SMF are compensated, the optical link becomes 160 km, 140 km for 3 and 7 users, respectively, where the BER attain less than 10^{-9} . In addition, Q-factor and eye opening are enhanced.

Conflict of Interest

The authors have not declared any conflict of interest.

REFERENCES

- Agrawal GP (1997). optical fiber communications systems, John Wiley.
- Aljunid SA, Ismail M, Ramli AR, Ali BM, Abdullah MK (2004). A new family of optical code sequences for spectral- amplitude coding optical CDMA systems. *Photonics Technol. Lett. IEEE*. 16:2383-2385.
- Al-Khafaji HMR, Aljunid SA, Fadhi HA (2012). Improved BER based on intensity noise alleviation using developed detection technique for incoherent SAC-OCDMA systems. *J. Modern Optics*. 59:878-886.
- Erdogan T, Mizrahi V, Lemaire PJ, Monroe D (1994). Decay of ultraviolet-induced fiber Bragg gratings. *J. Appl. Phys.* 76:73–80.
- Fadhil HA, Aljunid SA, Ahmad RB (2010). Design considerations of high performance optical code division multiple access: A new spectral amplitude code based on laser and light emitting diode light source. *Institution Eng. Technol.* 4(1):29-34.
- Hill KO, Fujii Y, Johnson DC, Kawasaki BS (1978). Photo sensitivity in optical fiber waveguides: Application to reflection filter fabrication. *Appl. Phys. Lett.* 32:647–649.
- Kavehrad M (1995). Optical Code-Division-Multiplexed Systems Based on Spectral Encoding of Noncoherent Sources. *IEEE* 0733-8724.
- Noshad M, Jamshidi K (2010). Code family for modified spectral-amplitude-coding OCDMA system and performance analysis. *IEEE/OSA J. Opt. Commun. Netw.* 2:344–354.
- Raad SF, Howraa M, Mohammad A (2012). Transmission Performance of optical Code Division Multiple Access Network Based on Spectral Amplitude Coding. *J. Emerging Trends Comput. Infor. Sci.* 3:3.
- Ranjan AM (2014). The performance improvement of OCDMA by FBG. *Int. J. Electrical Electronics Res.* ISSN 2348-6988 (online). 2(3):63-69.
- Shalaby HMM, Ghafouri-Shiraz H, Wei Z (2001). Modified Quadratic Congruence Codes for Fiber Bragg-Grating-Based Spectral- Amplitude-Coding Optical CDMA System. *IEEE/OSA J. Lightwave Technol.* 19(9):1274-1281.
- Shastri BJ, El-Sahn ZA, Zeng M, Kheder N, Rusch LA, Plant DV (2008). A standalone burst- mode receiver with clock and data recovery, clock phase alignment, and RS (255, 239) codes for SAC- OCDMA applications. *IEEE Photonics Technol. Lett.* 20:363-365.
- Smith EDJ, Blaikie RJ, Taylor DP (1998). Performance Enhancement Spectral Amplitude-Coding Optical CDMA using Pulse Position Modulation. *IEEE Trans. Commun.* 46(9):1176-1184.
- Smith EDJ, Blaikie RJ, Taylor DP (1998). Performance enhancement of spectral-amplitude-coding optical CDMA using pulse-position modulation. *Commun. IEEE Trans.* 46(9):1176-1185.
- S-Pin T (2003). Several Optical CDMA Spectral Codes Structured Over Arrayed-Waveguide and Fiber- Bragg Grating. *Tainan, N. C. K. U.* pp. 1-61.
- Stok A, Sargent EH (2000). Lighting the local area: Optical code-division multiple access and quality of service provisioning. *IEEE Network* 14:42–46.
- Tiwari A, Singh D (2013). Simulation of a 3 Gb/s SAC-OCDMA Based on Multi-Diagonal Code. *Int. J. Eng. Res.* ISSN: 2319-6890(online), 2347-5013 (print). 2(8):496-498.
- Yen CT, Cheng HC, Chang YT, Chen WB (2013). Performance analysis of Dual Unipolar/Bipolar Spectral Code in optical CDMA Systems. *J. Appl. Res. Technol.* P.11.
- Yin H, Richardson DJ (2007). Optical Code Division Multiple Access Communication Networks Theory and Applications Springer.

Full Length Research Paper

Geophysical assessment of potential hydrological units in hydrologically challenged geomaterials of Makurdi, Benue State, Nigeria

Daniel N. Obiora^{1*}, Johnson C. Ibuot¹ and Nyakno J. George²

¹Department of Physics and Astronomy, University of Nigeria, Nsukka, Enugu State, Nigeria.

²Department of Physics, Akwa Ibom State University, Ikot Akpaden, Nigeria.

Received 3 July, 2015; Accepted 10 August, 2015

A geo-electric survey employing the Vertical Electrical Sounding (VES) was carried out in order to access the distributions of electrical and hydraulic parameters of hydro-geologic units in some locations of Makurdi where groundwater resources are difficult to tap. A total of fifteen geo-electric soundings were acquired. The contour maps were generated using the results. From the bulk aquifer resistivity and water resistivity values, the formation factor was calculated and it ranges from 4.12 to 10.07. The porosity with a range of 24.58 to 39.36% and hydraulic conductivity with a range of 0.85 to 45.1 m/day were estimated. The porosity values confirm that hydro-geologic units in the study area consist mainly of sandstone. The high resistivity in the northern part of the study area is due to high water quality while the southern part has lower resistivity due to the presence of argillaceous materials. It is also observed that the areas with low resistivity have high porosity. The observed low resistivity zone with high porosity is believed to have poor interconnected pores, the condition for high total or absolute porosity in argillaceous materials. The analyses of the geophysical data constrained by geological and borehole information revealed that potable water can be extracted within the depth of 35 to 50 m in the study area.

Key words: Porosity, formation factor, hydraulic conductivity, aquifer resistivity, Makurdi, geo-electric survey.

INTRODUCTION

The increase in population and urbanization has led to an increase in the demand for groundwater by the populace in Makurdi. A greater percentage of the population depends on groundwater as the main supply of potable water. The study area located in the Benue trough has many challenges as regards to groundwater potential evaluation. The study area is located within the coastal

sedimentary lowlands of the middle Benue trough. Markurdi Sandstone occurs where Sandstones dominate and Sandstones are usually believed to be the best aquifers in terms of groundwater yield. The discontinuous nature of the water bearing system makes detailed knowledge of the subsurface geology, its weathering depth and structural disposition through geologic and

*Corresponding author. E-mail: daniel.obiora@unn.edu.ng, Tel: +2348038804735.

Author(s) agree that this article remain permanently open access under the terms of the [Creative Commons Attribution License 4.0 International License](https://creativecommons.org/licenses/by/4.0/)

geophysical investigations difficult. According to Edet and Okereke (1997) and Olorunfemi and Fasuyi (1993), weathering is an important factor that determines the presence of porosity and permeability.

Some researchers have used different techniques to estimate the spatial distribution of aquifer parameters such as hydraulic conductivity, transmissivity and aquifer depth (Allen et al., 1997). The hydraulic characteristics of subsurface geo-materials are important properties for groundwater assessments and also for safe construction of civil engineering structures (Pantelis et al., 2007). Groundwater recharge is dependent on rainfall and high porosity and connectivity of pore space of the water bearing units and as such the amount of groundwater in a formation is a function of porosity. The number of pores and crevices in a soil and rock and how well they are connected determines how easily groundwater moves through the ground and how much groundwater comes from a particular layer. Because groundwater has to move between pores and crevices in soil and rock, it moves much more slowly than surface water. The aquifer's electrical resistivity is mainly influenced by porosity and fluid resistivity in pores and the geo-electrical data recorded on the subsurface contains useful information about the aquifer which can be interpreted by experienced geophysicists for hydro-geological studies (Niwas and Celik, 2012).

The problem of estimating rock fluid and hydraulic properties becomes more important as hydrologists are asked to solve problems related to groundwater flow in rock materials about which little is known (Jorgensen, 1989). Hydraulic and electric conductivities are dependent on each other since the mechanisms of fluid flow and electric current conduction through porous media are governed by the same physical parameters and lithological attributes (Salem, 1999). The poor knowledge of the geometry and nature of the aquifers have posed problem to groundwater exploitation as many boreholes have been drilled without any knowledge of the hydro-geophysical characteristics and distribution of aquifers in the Makurdi Formation.

Transmissivities, formation factors and hydraulic conductivity can be estimated in a porous media using empirical/semi-empirical correlation, often using simple linear relations (Kelly, 1977; Heigold et al., 1979; Schimschal, 1981; Urish, 1981; Chen et al., 2001). The physical condition controlling the electric current flow also controls the flow of water in a porous media. Groundwater flow in fractured aquifers is very complicated and accuracy in estimation of the hydraulic parameters depends on the hydraulic behavior in a particular fracture, which is site specific (Singh, 2005). The choice of Vertical Electrical Sounding (VES) for the study is based on the fact that the electrical resistivity of most rocks depends on the amount of water in their pores and the distribution of these pores and the salinity of the water in them (Todd, 2004). The variation of conductivity

within the earth's subsurface layers affects the distribution of electric potential. The degree of this effect depends on the size, shape, location and bulk electrical resistivity of the subsurface layers. The bulk electrical resistivity depends on the mineralogy of the rock containing the fluids (Lowrie, 1997). This study is aimed at using the geo-electric attributes to define the aquifer geometry and to assess the variation of electric and hydraulic parameters in the study area in order to map out the area with high aquifer potential in the study area.

GEOLOGY AND HYDROGEOLOGY

The study area (Makurdi) is located along the Benue River bank. It lies between latitudes 7°40'N and 7°50'N of the Equator and between longitude 8°20'E and 8°40'E of the Greenwich Meridian, covering a total area of about 670 km². The town is drained by River Benue and its tributaries. The south bank has three flood plains namely: Wurukum, Wadata, and Idye. These areas are flooded in the rainy season and are highly populated. The Makurdi Formation comprises the Lower Makurdi Sandstone, the Upper Makurdi Sandstone and the Wadata limestone. Makurdi lies within the Guinea savannah vegetation zone with a few patches of forests. The annual rainfall ranges between 1,500 to 2,000 mm with its peak rainfall in the months of July and September. Temperatures in March and April are about 38 and 48°C respectively, while in December/January, the temperature is about 27°C (Benue State Water Supply and Sanitation Agency, 2008). The area is accessible through Nassarawa, Taraba, Obudu, Enugu, and Ankpa road. Also, a good road network exists within Makurdi metropolis and a railway line running through the town from Enugu to Jos and Kaduna. The area can also be accessible through the Benue River which flows through from the Cameroon Mountain to the Niger-Benue confluence at Lokoja. Makurdi, belongs to the Makurdi Formation which overlies the Albian Shale. It consists of thick current bedded coarse grained deposits. The Makurdi Sandstone has a thickness of about 900 m (Offodile, 1976). The southern part of the Benue valley is generally gently undulating and punctuated by a few low hills. But toward the northeast, the relief is exaggerated by hills like the Lammuder and Ligri hills, which rise up to 600m above sea level. Figure 1 shows the geological map of Benue State.

Geologically, the Benue valley consists of a linear stretch of Sedimentary Basin running from about the present confluence of the Niger and the Benue rivers to the north east, and is bounded roughly by the Basement Complex areas in the north and south of the River (Figure 1).

MATERIALS AND METHODS

A direct current resistivity survey using the VES method was carried out in the study area. The VES is based on measuring the

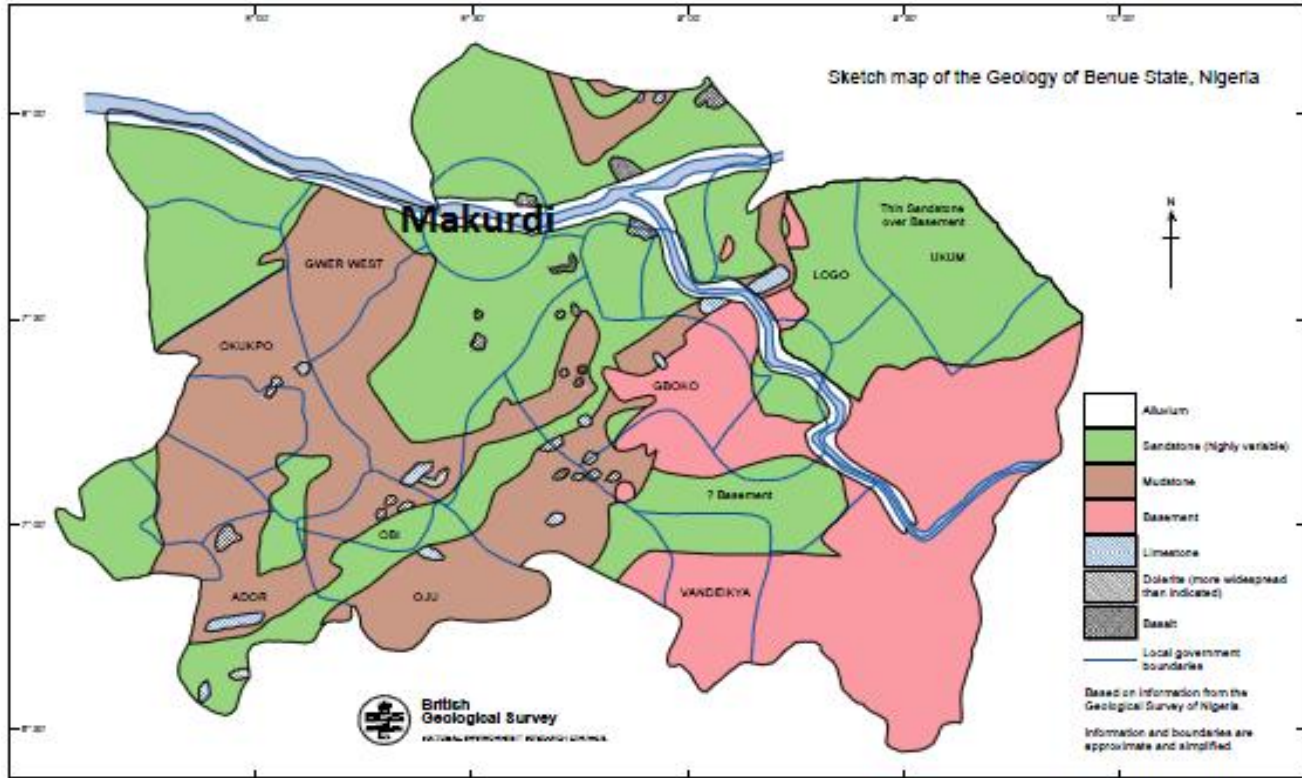


Figure 1. Geological Map of Benue State (British Geological survey 2001).

potentials between one electrode pair while transmitting direct current between another electrode pair. The Schlumberger array was chosen due to its better lateral resolution. The Schlumberger soundings were carried out with maximum half-current electrode spacing $\left(\frac{AB}{2}\right)$ of 100 m and potential electrode $\left(\frac{MN}{2}\right)$ of 15.0 m.

The PZ-02 resistivity meter was used to acquire the resistivity data by moving two or four of the electrodes used between each measurement. The survey was completed with 15 soundings. The apparent resistivity (ρ_a) was calculated using:

$$\rho_a = \pi \cdot \left[\frac{\left(\frac{AB}{2}\right)^2 - \left(\frac{MN}{2}\right)^2}{MN} \right] \cdot R_a \tag{1}$$

Where AB is the distance between the two current electrodes, MN is the distance between the potential electrodes, and R_a is the apparent electrical resistance measured from the equipment. The equation can be simplified to:

$$\rho_a = K \cdot R_a \tag{2}$$

Where K is the geometric factor : $\pi \cdot \left[\frac{\left(\frac{AB}{2}\right)^2 - \left(\frac{MN}{2}\right)^2}{MN} \right]$

Using the conventional partial curve matching technique with two-layer master curves in conjunction with auxiliary point diagrams (Orellana and Mooney, 1966), the initial estimates of VES data was achieved. From this, estimates of layer resistivities and thicknesses were obtained which served as starting points for computer-assisted interpretation. The conventional curves and auxiliary point diagrams (theoretical curves) used in the interpretation helped in obtaining a good fit between the observed field curves and the theoretical curves during total and partial matching. The computer software program, WINRESIST version 1.0 (one of the geophysical software used to process electrical resistivity data) was used and the data sets obtained from the manual interpretation stage were keyed as inputs into the computer modeling software (WINRESIST) to generate data for the estimated model. Examples of typical modeled VES curves constrained by borehole information were obtained within the study area as shown in Figures 2 to 5. The estimate of geo-electric layers was obtained from the quantitative interpretations of vertical electrical sounding data whose fidelity was validated by the use of typical borehole information (Figure 6). From this, aquifer depth, thickness and curve frequency were identified. The hydraulic conductivity was estimated using the equation as given by Heigold et al. (1979):

$$K = 386.40 R_{rw}^{-.93283} \tag{3}$$

Where K is the hydraulic conductivity, R_{rw} is the aquifer resistivity.

Rocks resistivity depends on the lithology and mineralization of water filling the pores. According to Archie's law 1942, the resistivity of aquifer (saturated rock) is directly proportional to the resistivity of water filling the pores:

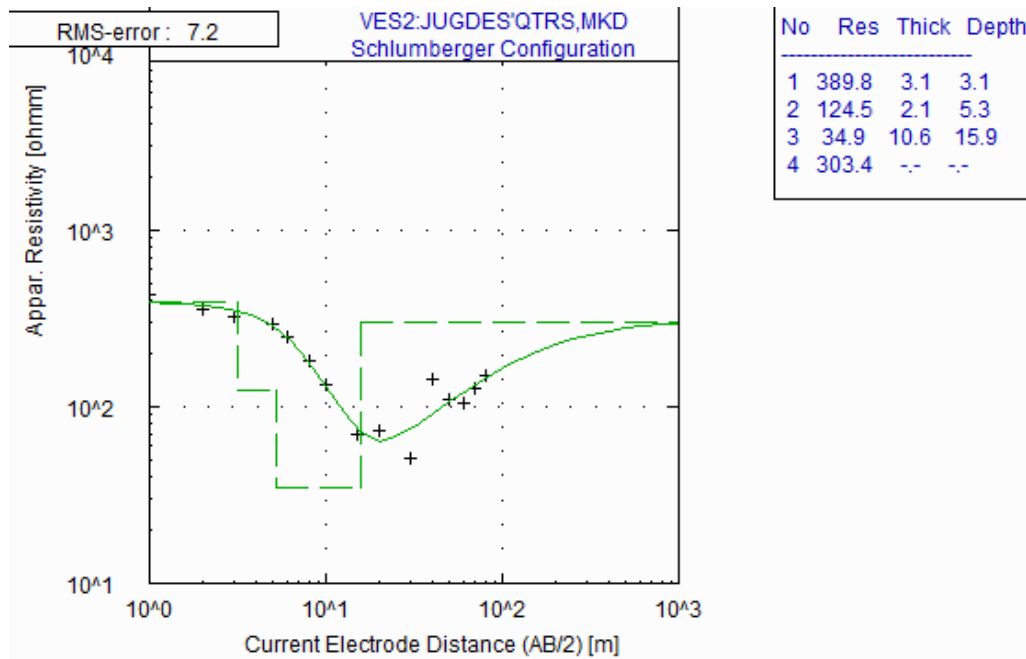


Figure 2. VES 1 Geoelectric curve.

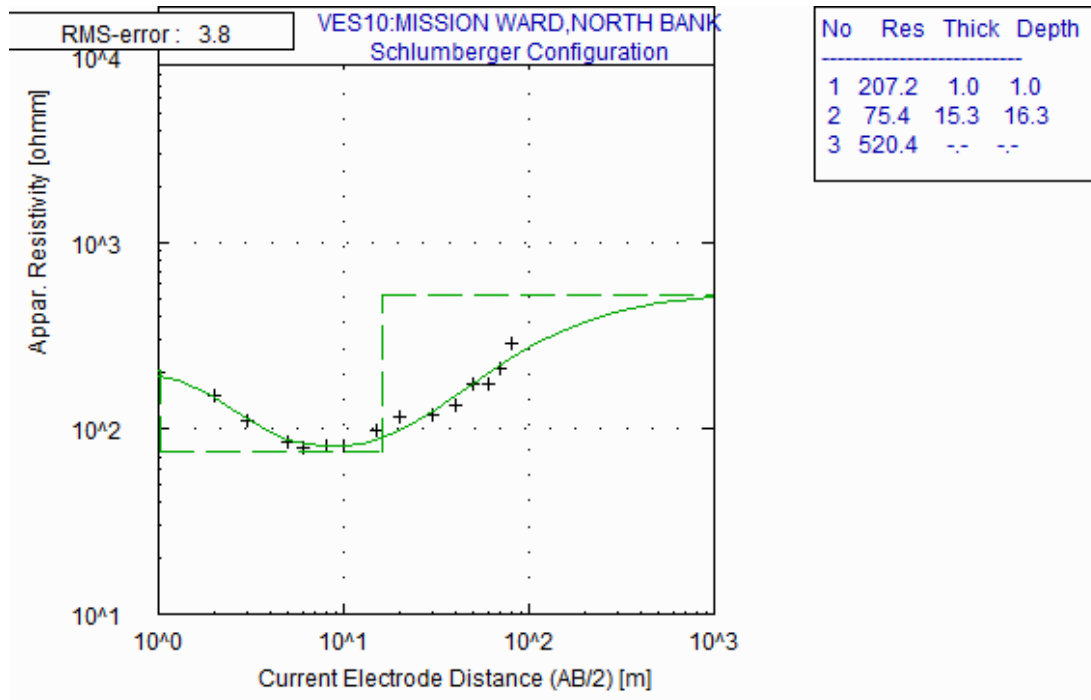


Figure 3. VES 5 Geoelectric curve.

$$\rho_a = F\rho_w \tag{4}$$

Where ρ_a is the aquifer resistivity, ρ_w is the water resistivity, F is

the Formation factor.

If a Formation factor is calculated from Equation (4), the apparent Formation factor is observed with increasing water resistivity. Formation factor (F) combines all the properties of the material influencing electrical current flow like porosity (Φ), pore shape, etc.

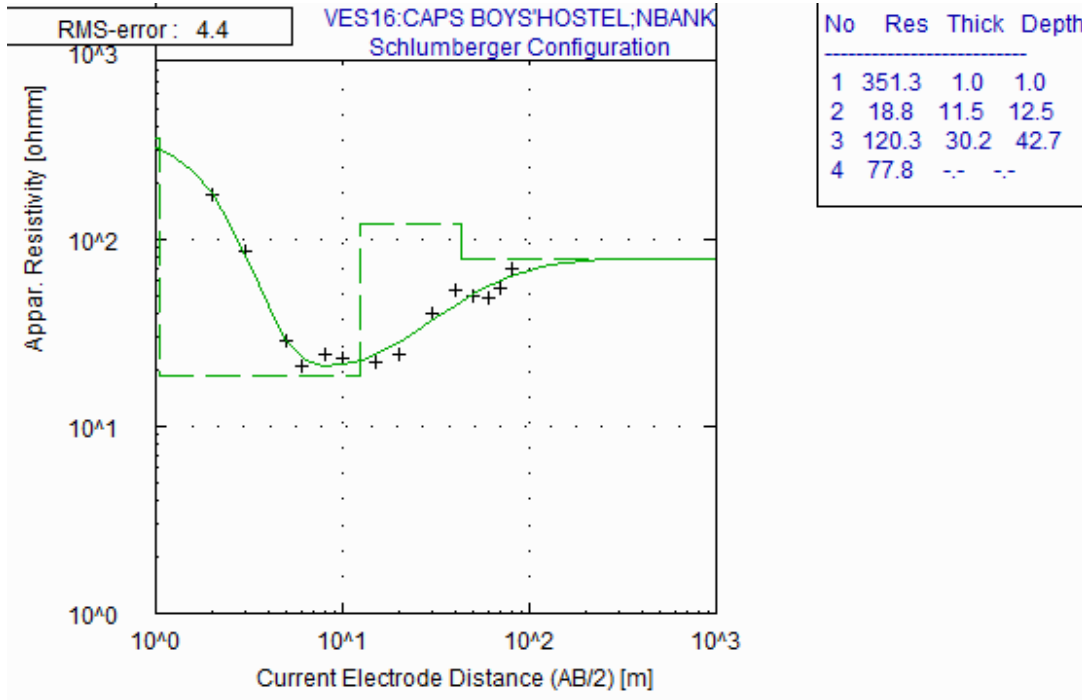


Figure 4. VES 8 Geoelectric curve.

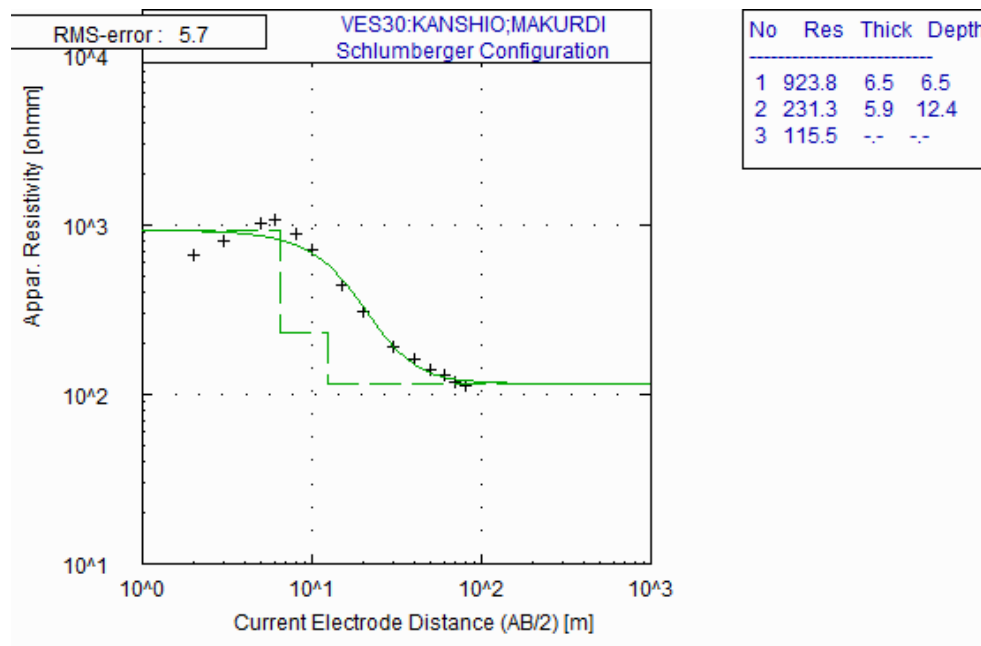


Figure 5. VES 15 Geoelectric curve.

$$F = a\phi^{-m} \tag{5}$$

Where a (0.7) is the average geometry factor and m (1.9) is the average cementation exponent for the study area being a sandstone region. From Equation (5), porosity is estimated.

RESULTS AND DISCUSSION

The summary of the VES results of fifteen geo-electrical soundings and the calculated hydraulic parameters of the aquifer layer is shown in Table 1. The interpreted curve

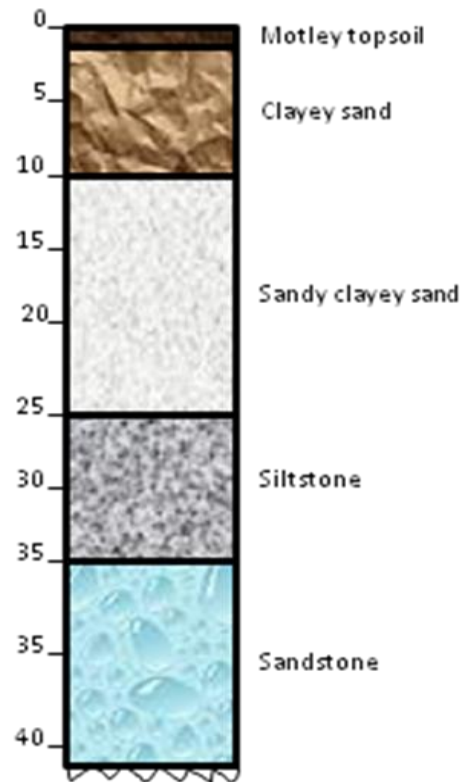


Figure 6. Typical borehole in the study area.

Table 1. Summary of results of geo-electric and hydraulic parameters.

VES station	Location name	Long. (deg)	Lat. (deg)	Aquifer resistivity (ρ_a) (Ωm)	Water resistivity (ρ_w) (Ωm)	Formation factor (F)	Porosity (ϕ)(%)	Hydraulic conductivity (K) ($mday^{-1}$)	VES curve types
1	Judges Qtrs	7.7123	8.5780	82	16.3	5.03	35.42	6.34	QH
2	Owner,s occupier	7.6964	8.5486	135	21.3	6.34	31.36	3.98	KQ
3	Nyiman layout	7.6963	8.5448	72	15.6	4.62	37.06	7.15	KQ
4	Nyiman layout	7.7053	8.5153	273	28.2	9.68	25.09	2.06	KQ
5	High level	7.7184	8.5225	131	19.5	6.72	30.42	4.09	AA
6	Industrial Estate	7.7020	8.4901	10	2.4	4.12	39.36	45.1	H
7	UniAgric road	7.7631	8.5753	31	5.7	5.44	33.99	15.7	HK
8	CAPS Staff Qtrs	7.7726	8.5958	39	6.4	6.09	32.02	8.75	A
9	Shamija village	7.7623	8.6181	304	32.9	9.24	25.72	1.87	KQ
10	Uchonu village	7.7706	8.5510	271	27.6	9.82	24.91	2.08	KQ
11	Wadata	7.7444	8.5155	39	6.9	5.65	33.31	12.67	QH
12	Ankpa Qtrs	7.7096	8.5040	46	7.8	5.90	32.57	10.44	Q
13	New GRA	7.6872	8.5388	702	69.7	10.07	24.58	0.85	K
14	Kanshio	7.6834	8.5367	150	24.6	6.01	32.01	3.61	QH
15	Lower Staff Qtrs	7.6606	8.5592	160	25.8	6.20	31.72	3.4	HK
	Average			163.0	20.71	6.73	31.30	8.54	

types show that the study area is characterized by seven sounding curve types; QH, KQ, AA, H, HK, A, Q, and KQ-

curve types. Geo-electric curve type is the use of letters H, K, A and Q to describe the relation between layer

Table 2. Ranges of porosity in typical earth materials (Driscoll, 1986; Freeze and Cherry, 1979; Roscoe Moss, 1990).

Consolidated rock	Porosity (%)
Sandstone	5 - 35
Limestone/Dolomite	< 1 - 20
Shale	< 1 - 10
Crystalline rock (fractured)	< 1 - 5
Vesicular basalt	5 - 10

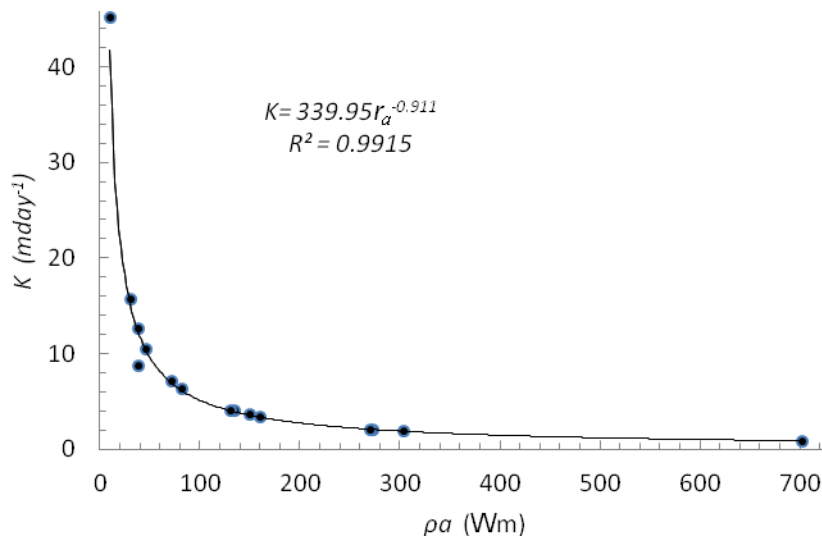


Figure 7. A graph of hydraulic conductivity against aquifer bulk resistivity.

resistivities in a geo-electric section. It indicates that electrical sounding curve is obtained over a geoelectric section in which the layer resistivities varies (Zohdy et al., 1990). The bulk aquifer resistivity (ρ_a) with an average of 163 Ωm ranges from 10 to 702 Ωm . The water resistivity ranges from 2.4 to 69.7 Ωm with an average value of 20.71 Ωm . The aquifer formation factor (F) calculated from the bulk aquifer resistivity and water resistivity ranges from 4.12 to 10.07 and its average value calculated as 6.73. The aquifer porosity was estimated to range from 24.58 to 39.36% with an average of 31.35%. This shows that the aquifer in the study area is dominated by sandstone (Table 2). The hydraulic conductivity is highly variable and is observed to decrease as resistivity increases. The hydraulic conductivity ranges from 0.85 to 45.1 m/day and its average value is 8.54 m/day.

The calculated hydraulic conductivity (K) was plotted against aquifer resistivity (ρ_a), where an inverse relationship was obtained between the two variables (Figure 7). The relationship between aquifer resistivity and water resistivity is shown in Figure 8. A linear relationship between the two variables is obtained which

shows that aquifer resistivity increases in direct proportional to water resistivity with a strong correlation coefficient:

$$\rho_a = 10.41\rho_w - 52.80 \tag{6}$$

From the results in Table 1, contour maps were generated. The aquifer contour map (Figure 9) shows the distribution of aquifer resistivity in the study area. It can be seen that conductivity (inverse of resistivity) is high at the southern part of the study area and it increases gradually towards the northeastern part with low conductivity observed in the extreme north through northwest down to part of the southwest, thus resistivity increases towards the northern part of the study area. This means that the geo-materials in the northern part are highly resistive (low conductive minerals) and the aquifer is saturated and thus a high groundwater quality. VES 13 (New GRA) has the highest resistivity value of 702 Ωm while the least 10 Ωm is observed in VES 6 (Industrial Estate) indicating shale/clay signatures. From the average value of 163 Ωm , it can be inferred that the study area is more of Sandstone intercalated with clay.

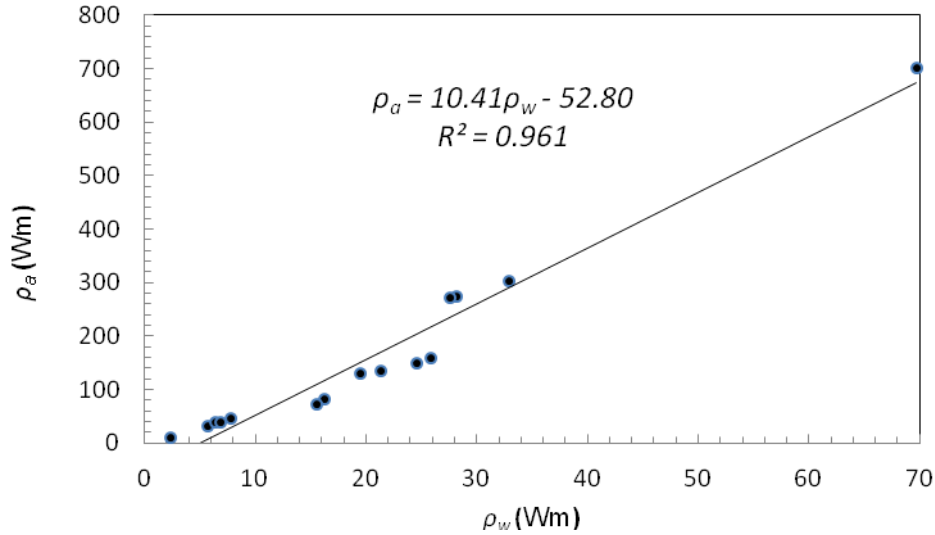


Figure 8. A graph of aquifer bulk resistivity against water resistivity.

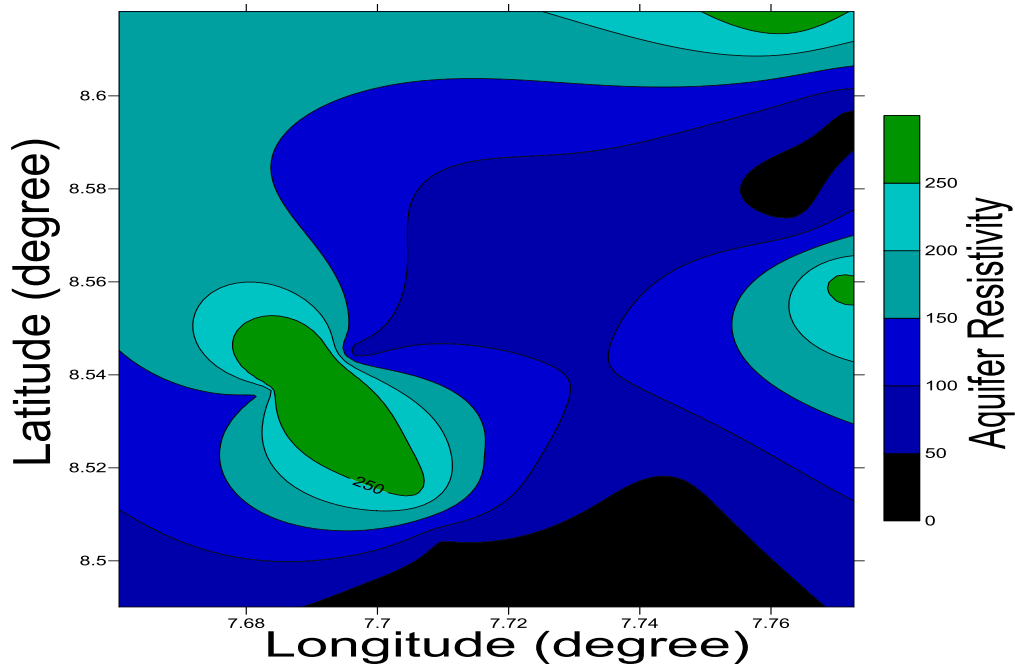


Figure 9. Contour map showing the distribution of aquifer resistivity in the study area.

The variation of aquifer water resistivity is directly proportional to that of aquifer bulk resistivity. Figure 10 shows a gradual increase in water resistivity from south towards the northern part of the study area. This indicates that the southern part of the study area will have highly conductive ions. Areas with low aquifer formation factor correspond to areas with low aquifer bulk resistivity. The distribution of formation factor (ratio of bulk aquifer resistivity to water resistivity) is shown in Figure 11. A decrease of the formation factor is observed

with increasing aquifer bulk and water resistivity. The range of porosity in the study area revealed that the study area is dominated with Sandstone with the mean value being 31.3%. Variation of porosity is shown in Figure 12. The highest porosity value is observed in VES 6 (Industrial Estate) with a value of 39.36%. It can thus be inferred that high porosities are associated with aquifers of relatively low aquifer resistivity values and also it suggests high storativity of the aquifer in the area. From the contour map (Figure 12), porosity is high at the

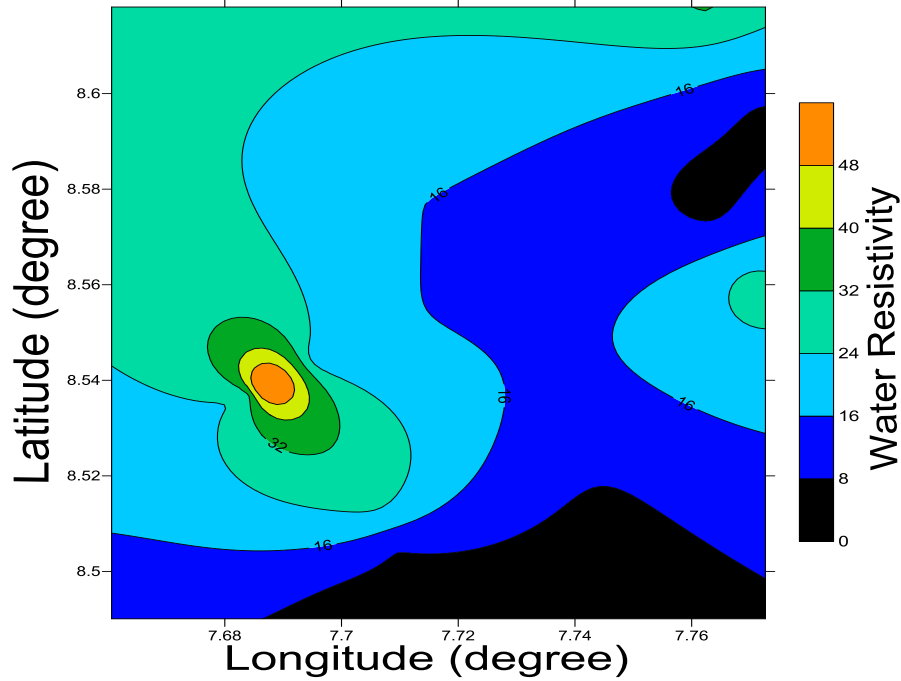


Figure 10. Contour map of showing distribution of water resistivity.

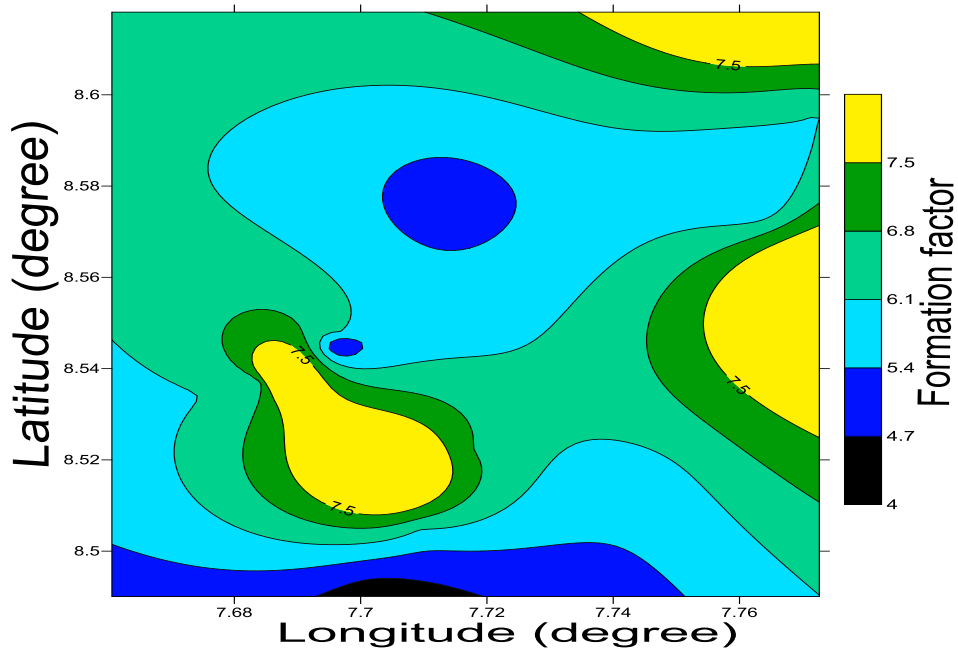


Figure 11. Contour map showing the distribution of Formation factor.

extreme south and the central parts of the study area. Increase or decrease in porosity leads to a corresponding increase or decrease in hydraulic conductivity (K). Figure 13 shows the variation of hydraulic conductivity in the study area which is revealed to be highly variable (0.85 to

45.1 m/day). Hydraulic conductivity increases in the north-south direction as shown on the contour map. The hydraulic conductivity controls the behavior of groundwater flow within an aquifer. It is observed from this study that, increase in resistivity lowers the hydraulic

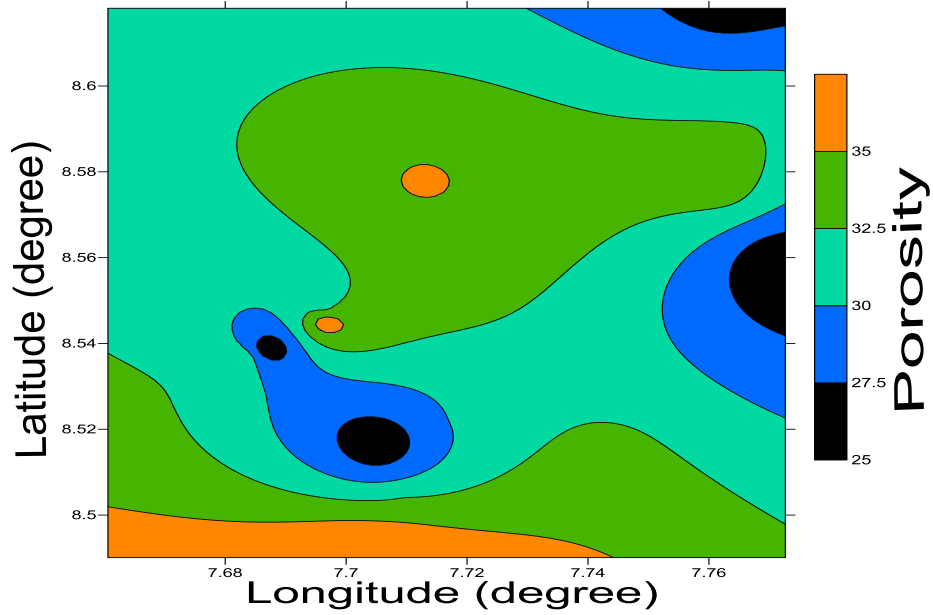


Figure 12. Contour map of the study area showing the variation of porosity.

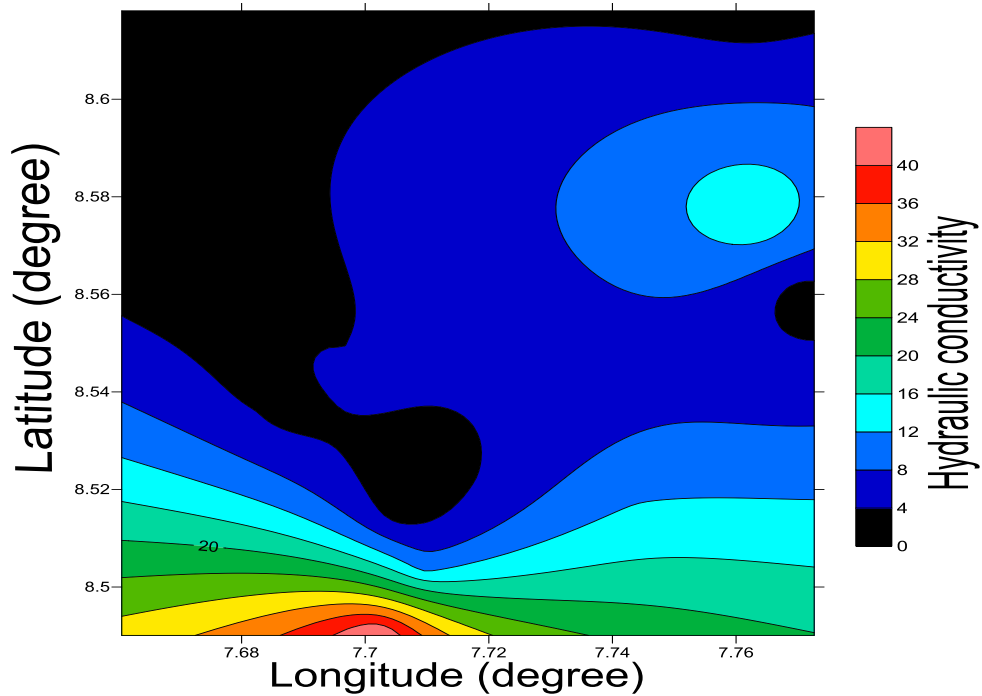


Figure 13. Contour map showing variation of hydraulic conductivity.

conductivity of the aquifer geo-materials.

Conclusion

Fifteen VES were used for this study to evaluate the geo-

electric and hydraulic conditions of the study area. There is a good correlation existing between aquifer bulk resistivity and water resistivity. The results indicate the presence of aquifer consisting mainly of Sandstone. The contour maps show increase in both bulk aquifer and water resistivities towards the north. The study revealed

that areas with relatively low aquifer resistivity have high porosity values, which indicates high storativity. The porosity is high in the southern and central parts of the study area. It is also observed that hydraulic conductivity decreases as resistivity increases in the area. The area characterized by high porosity but low resistivity is believed to have poor communicating pores and there could not be regarded as potential aquifers. The low resistivity with high absolute porosity zone indicates the presence of argillaceous materials. The use of vertical electrical sounding technique provides geo-electrical and geo-hydraulic information that can be used in resolving the existing challenge in the extraction of groundwater in Makurdi Formation. The estimated contour distributions and simulated models can improve the extraction of potable subsurface water in the study area.

Conflict of Interest

The authors have not declared any conflict of interest.

ACKNOWLEDGEMENTS

The authors are grateful to Dr. Josiah Chukudebelu and Mr. Adeolu Ajala, both of Department of Physics and Astronomy, University of Nigeria, Nsukka, for their useful contributions.

REFERENCES

- Allen DJ, Brewerton LJ, Coleby LM, Gibb BR, Lewis MA, MacDonald MA, Wagstaff SA, Williams AT (1997). The physical properties of major aquifers in England and Wales. British Geological Survey Technical Report, WD/97/34.
- Archie GE (1942). The electrical resistivity logs as an aid in determining some reservoir characteristics. *Trans. Am. Inst. Mineral. Metallurgical Eng.* 146:54-62.
- Benue State Water Supply and Sanitation Agency (2008). Unpublished Report.
- British geological survey (2001). Sketch map of the geology of Benue State; Report on visit to a Water Aid project, Nigeria, to carry out workshops and assess geology of Benue State. Keyworth Nottingham.
- Chen J, Hubbard S, Rubin Y (2001). Estimating the hydraulic conductivity at the south Oyster site from geophysical tomographic data using Bayesian techniques based on the normal linear regression model. *Water Resour. Res.* 37(6):1603–1613.
- Driscoll F (1986). *Groundwater and wells*. Johnson Screens, St Paul, Minnesota.
- Edet AE, Okereke CS (1997). Assessment of hydrogeological conditions in basement aquifers of the Precambrian Oban massif south-eastern Nigeria. *J. Appl. Geophys.* 36(4):195-204.
- Freeze A, Cherry J (1979). *Groundwater*. Prentice-Hall, Upper Saddle River, NJ.
- Heigold PC, Gilkeson RH, Cartwright K, Reed PC (1979). Aquifer Transmissivity from surficial Electrical methods. *Ground Water.* 17(4):338–345.
- Jorgensen DG (1989). Using Geophysical Logs to Estimate Porosity, Water Resistivity and Intrinsic Permeability. US Geological Survey Water-supply paper. 2321.
- Kelly WE (1977). Geoelectric Sounding for Estimating Aquifer Hydraulic Conductivity. *Ground Water.* 16(6):420-425.
- Lowrie W (1997). *Fundamentals of Geophysics*. Cambridge University Press, New York.
- Niwas S, Celik M (2012). Equation Estimation of Porosity and Hydraulic conductivity of Ruhrtal aquifer in Germany using near Surface Geophysics. *J. Appl. Geophys.* 84:77-85.
- Offodile ME (1976). A Review of the Geology of the Cretaceous of the Benue Valley. In: *Geology of Nigeria*, ed. Kogbe CA. Elizabethan Publishing Company, Lagos, Nigeria. pp. 319-330.
- Olorunfemi MO, Fasuyi SA (1993). Aquifer Types and the Geoelectric/Hydrogeologic Characteristics of Part of Central Basement Terrain of Nigeria (Niger State). *J. Afr. Earth Sci.* 16(3):309-317.
- Orellana E, Mooney H (1966). *Master Tables and Curves for VES over Layered Structures*. Interciencia, Madrid, Spain.
- Pantelis MS, Maria K, Fillippos V, Antonis V, George S (2007). Estimation of Aquifer Hydraulic Parameters from Surficial Geophysical methods. *J. Hydrol.* 338:122-131.
- Roscoe Moss Company (1990). *Handbook of Ground Water Development*. John Wiley and Sons, New York.
- Salem HS (1999). Determination of Fluid Transmissivity and Electric Transverse Resistance for shallow Aquifers and deep reservoirs from Surface and well-log electric measurements. *Hydrol. Earth System Sci.* 3(3):421-427.
- Schimschal U (1981). The relationship of geophysical measurements to hydraulic conductivity at the Brantley dam site, New Mexico. *Geoexploration.* 19:115–125.
- Singh KP (2005). Nonlinear estimation of aquifer parameters from surficial resistivity measurements. *Hydrol. Earth Syst. Sci. Discussions.* 2:917-993.
- Todd DK (2004). *Groundwater Hydrology*, 2nd Edition. John Wiley and Sons, New York.
- Urish DW (1981). Electrical resistivity-hydraulic conductivity relationships in glacial outwash aquifers. *Water Resour. Res.* 17(5):1401-1408.
- Zohdy AAR, Eaton GP, Mabey DR (1990). *Techniques of Water-Resources Investigations of the United States Geological Survey*. U.S. Geological Survey, Denver.

Full Length Research Paper

Effect of tempering on the microstructure and mechanical properties of austenitic dual phase steel

Sunday Chukwuyem IKPESENI^{1, 2*}, Obimma Basil ONYEKPE² and Monday Itopa MOMOH³

¹Department of Mechanical/Metallurgical Engineering, Delta State University, Abraka, 740005, Nigeria.

²Department of Mechanical Engineering, University of Benin, Benin-City, 300271, Nigeria.

³Department of Metallurgical Engineering, Kogi State Polytechnic, Lokoja, 270001, Nigeria.

Received 10 June, 2015; Accepted 4 August, 2015

This research is focused on the effect of tempering on the microstructure and mechanical properties of 0.23%C austenitic dual phase steel locally manufactured in Nigeria. The as-received steel was normalized in order to annul the thermo-mechanical history of the steel. Thereafter, some of the normalized samples were austenitized at 850°C for 30 min and then slowly cooled in the furnace to the ($\alpha+\gamma$) region and soaked for 30 min each at 790, 770, 750 and 730°C; and then quenched in hot water at 50°C. Again, some of the as-step quenched samples were tempered at 320°C for 1 h and air cooled. Mechanical testing and microstructures studies were conducted on all the heat treated samples. Optimum combination of properties was observed with samples intercritically step quenched at 770°C and tempered at 320°C for 1 h. Its hardness, impact strength, total elongation and ultimate tensile strength improved from 241.45 to 327.15 Hv, 0.26 to 1.66 J/mm², 9.14 to 36.03% and 785.68 to 1569.28 N/mm² respectively over the as-step quenched steel; representing 35.49, 538.46, 294.20 and 99.74% respectively. Microstructure photographs revealed duplex microstructure essentially comprised of ferrite and martensite with dispersion of carbide or retained austenite which is a typical characteristic of conventional dual phase steels.

Key words: Tempering, austenitic dual phase steel, mechanical properties, microstructures.

INTRODUCTION

The development of new materials with improved properties has remained the hallmark of the progress and breaks through made in technological advancement. Over the past three decades research in micro alloy steel has been directed towards the development of a new class of High Strength Low-Alloy (HSLA) steels known as Advanced High-Strength Steels (AHSS). This class of steel have been used in the automotive industry as a

solution for weight reduction, safety performance improvement and cost saving. Among them, the dual phase steels (DPS), whose microstructure consists of mainly ferrite and martensite, are an excellent choice for applications where low yield strength, high tensile strength, continuous yielding and good uniform elongation are required. Their potential as superior strength and formability substitutes for current automotive

*Corresponding author. E-mail: sunnychukwuyem@yahoo.com

Author(s) agree that this article remain permanently open access under the terms of the [Creative Commons Attribution License 4.0 International License](https://creativecommons.org/licenses/by/4.0/)

Table 1. Chemical composition analysis result.

Element	C	Si	Mn	S	P	Cr	Ni	Cu	Fe
Weight (%)	0.23	0.20	0.73	0.03	0.03	0.12	0.10	0.27	98.30

steels was recognized and has provided an incentive for their rapid development and acceptance in this role (Sang et al., 2006; Bello et al., 2007; Zhao et al., 2009).

Recently, several researches have been conducted to determine the effect of temperature on the size and volume of the hard phase (martensite) and properties (Zhao et al., 2009; Offor et al., 2010; Daramola et al., 2010; Yazici et al., 2009; Mohammad and Ekarami, 2008). Among other notable researchers, Smallman (1995) studied and reported that the flow stress and tensile strength of these steels increase with a corresponding decrease in ductility with about 20% volume fraction of the martensite producing the optimum properties. However, Bag and the associates has shown that dual phase steels containing approximately equal amounts of finely dispersed ferrite and martensite phases (50 to 60%), exhibit the optimum combinations of high strength and ductility with impact toughness (Bag et al., 1999). Alaneme and the group also reported that better combination of fatigue and tensile properties were obtained at 760 and 780°C compared to 740°C. They attributed the improved mechanical properties to increased volume fraction of martensite (Alaneme et al., 2010). In the same line of reasoning, Majid observed that dual phase steels with equal amount of ferrite and martensite have excellent mechanical properties. He also reported that volume fraction of martensite increases with temperature (Majid, 2010).

In general, literature review has reported that the optimum intercritical annealing temperature lies between 760 and 790°C depending on the composition of the steel. All attested to the fact that dual phase steels possess superior properties when compared with normalized steels and quenched and tempered steels.

In spite of this observations and unique properties exhibited by dual phase steel, little has however been experimented on the steel's reaction(s) to tempering after development. This thus serves as impetus to this research as it focused on examining the effect of tempering on the microstructure and mechanical properties of austenitic dual phase steel. Austenitic dual phase steels are those dual phase steels with austenite as the starting microstructure during development or production (that is, the product of step quenching intercritical annealing process).

MATERIALS AND METHODS

The material for this investigation is a carbon steel, as-supplied in cylindrical form of 16 mm diameter. The chemical composition of

the steel shown in Table 1 was performed using spectrometric analyzer (NCS Labspark 750B).

Heat treatment

All initially machined samples were normalized at 850°C (30°C above AC_3) and held for 60 min in a muffle furnace. A group of these normalized samples were labelled as "A" and used as control. The other group of normalized samples were subjected to step-quenching intercritical annealing treatment in order to produce the austenitic dual phase steel. This involved heating to austenitic temperature of 850°C and soaking for 1 h, followed by slow cooling in the furnace to the dual phase ($\alpha + \gamma$) region, soaked for 30 min at different temperatures and then quenched in water. This is followed by subjecting some of the step-quenched samples to tempering operation at 320°C for 1 h and air cooled. All samples were designated as shown in Table 2.

Sample preparation and testing

After the heat treatment operations, all samples at their respective test configurations were separated and properly designated prior to tests and analysis. The impact test was conducted by means of a pendulum charpy impact tester. All the samples were tested to fracture at room temperature. The hardness of the samples was determined using a microhardness tester with inbuilt display unit. The tensile properties of the samples were determined using the Instron 3369 universal tester fitted with computer interface. The specimens were prepared to ASTM standard (ASTM E8M-91, 1992).

Small samples cut from the heat treated samples were metallographically prepared for microstructural examination following standard procedures. The fractured surfaces of some fractured impact samples were examined using the scanning electron microscope (SEM).

RESULTS AND DISCUSSION

Intercritical annealing temperature and the mechanical properties of intercritically annealed step quenched samples

With austenite as the starting microstructure for this intercritical annealing, Figure 1 reveals that the hardness of the as-step-quenched samples (series G) is rising and falling with samples annealed at 790°C having the highest hardness value while minimum value is observed at 770°C. The high hardness recorded at 790°C could be attributed to high volume martensite content as a result of more austenite which transforms to martensite on quenching from that temperature.

Figure 2 shows that there is a decrease in the UTS above 750°C after an initial increase. The initial rise in

Table 2. Identification code of samples.

Type of heat treatment	Temperature (°C)	Identification code
Normalizing	850	A
	730	G730
	750	G750
Step quenching	770	G770
	790	G790
	730	G730T
Tempered step quenched samples	750	G750T
	770	G770T

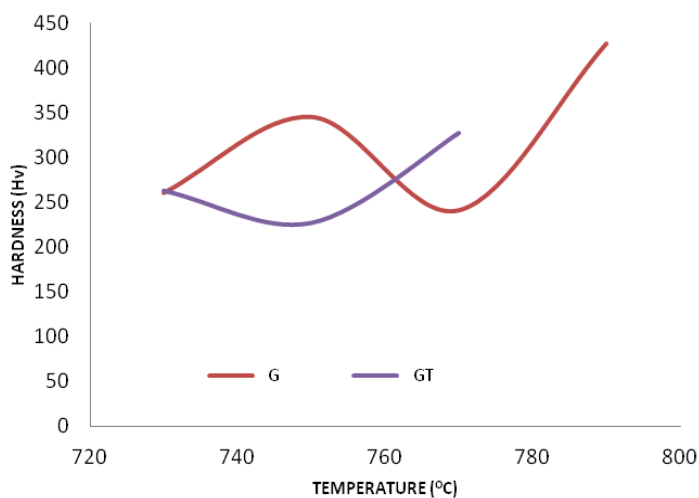


Figure 1. Hardness value versus temperature.

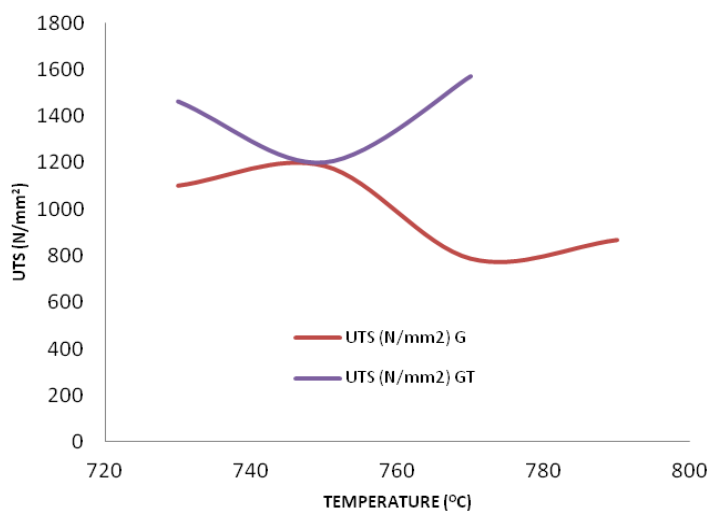


Figure 2. Ultimate tensile strength versus temperature.

UTS could be attributed to grain refinement after 730°C as evident in Figure 5 (a) and (c). The fall in UTS at

higher temperatures could be attributed to very high martensite volume fraction, because at higher

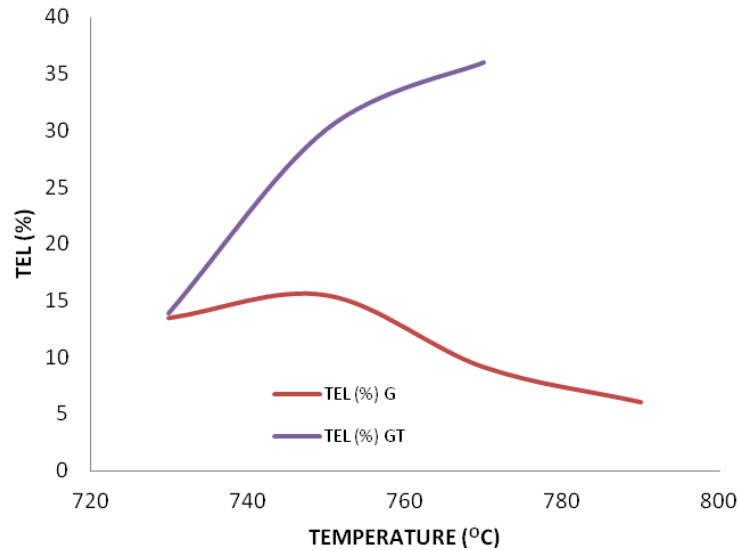


Figure 3. Total elongation versus temperature.

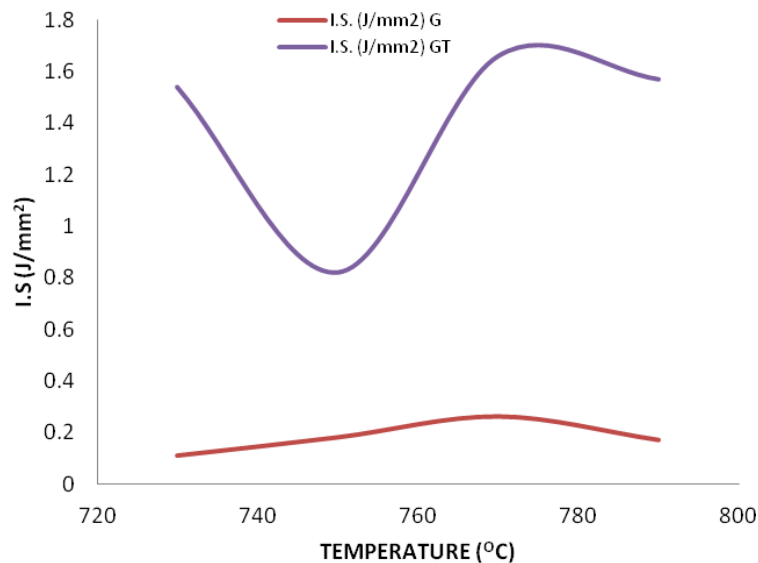


Figure 4. Impact strength versus temperature.

temperatures the amount of austenite is quite high which upon quenching transforms to martensite. Carbon content increases with increased temperature and this affects mechanical properties adversely. While at lower temperatures ferrite would have precipitated out from the prior austenite which most likely reduces the amount of martensite to or near the optimum amount for high strength. Also the grain refinement observed at 750°C creates obstacles to movement of dislocation which in turn requires more stress. Total elongation (TEL) also follows the same trend with UTS (Figure 3). It has also been reported that the carbon content of martensite

decreases with increased volume fraction of martensite; this has a detrimental effect on ductility above 50%. It is pertinent to note that TEL at all temperature fell below the normalized sample. There is a steady increase in impact strength of sample given the same treatment with increased temperature as depicted in Figure 4 (series G). Though, all the impact strength values obtained are very poor compared to the normalized steel sample. Results shown in Table 3 proved that intercritical step quenching does not favour the improvement of ductility and impact strength at all the investigated temperatures. However, the optimum temperature for properties is at 750°C for

Table 3. Summary of the mechanical properties of the developed DPS.

Sample	UTS (MPa)	Y.S (MPa)	Y.S/U.T.S	TEL (%)	I.S (J/mm ²)	Hd (Hv)
A	670.55	385.96	0.575	21.97	1.30	161.7
G730	1099.6	351.87	0.32	13.43	0.11	260.75
G750	1184.64	-	-	15.43	0.18	345.1
G770	785.68	-	-	9.14	0.26	241.45
G790	866.1	-	-	6.06	0.17	426.5
G730T	1462.32	921.26	0.63	13.85	1.54	262.75
G750T	1202.68	817.82	0.68	30.1	0.82	226.85
G770T	1569.28	816.03	0.52	36.03	1.66	327.15

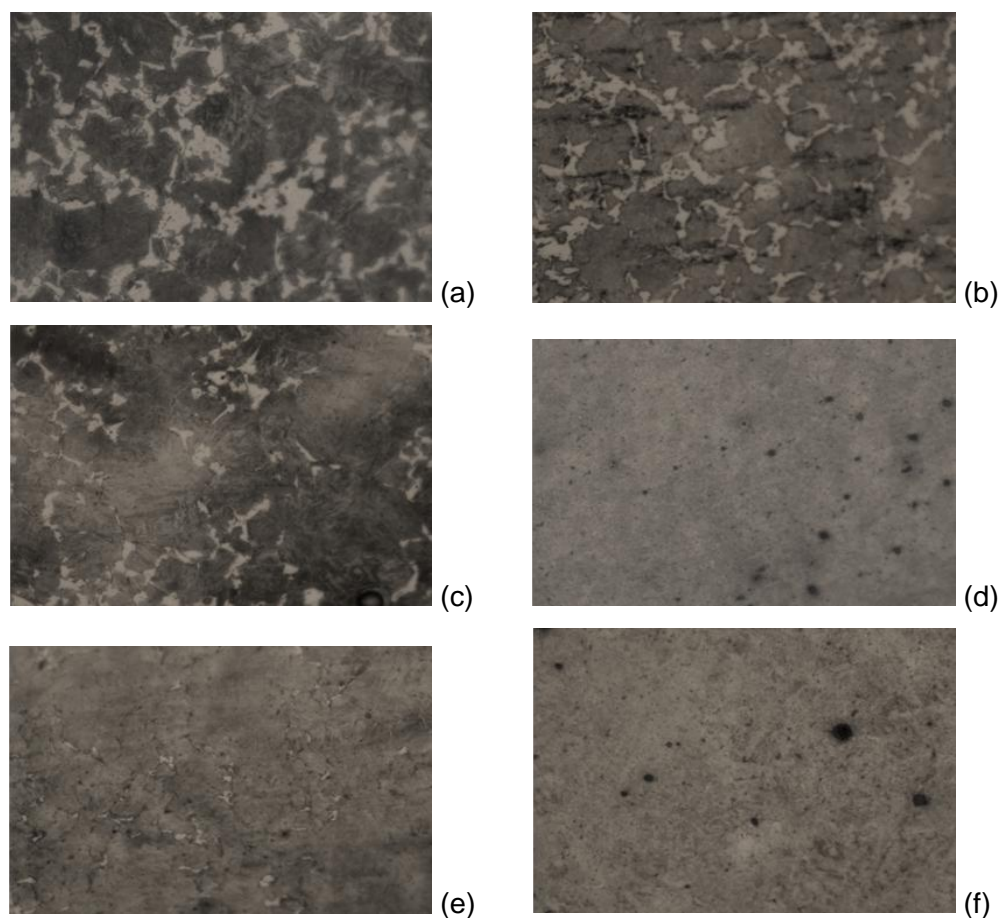


Figure 5. (a) G730 X200. Sample step quenched at 730°C for 30 min. (b) G730T X200. Sample step quenched at 730°C for 30 min and tempered for 1 h at 320°C. (c) G750 X200. Sample step quenched at 750°C for 30 min. (d) G750T X200. Sample step quenched at 750°C for 30 min and tempered for 1 hour at 320°C. (e) G770 X200. Sample step quenched at 770°C for 30 min. (f) G770T X200. Sample step quenched at 770°C for 30 min and tempered for 1 hour at 320°C.

the step quenching intercritical annealing heat treatment. The performance of UTS, hardness, impact strength and total elongation relative to the normalized sample at 750°C are 76.67, 113.42, -86.15 and -29.77% respectively. The negative signs indicate deterioration of property.

Microstructure evolution with temperature for samples intercritically step quenched

Figure 5(a), (c) and (e) are the photomicrographs of the samples that were subjected to “Step Quench” operation with austenite as the initial microstructure. The rather

Table 4. comparison of properties' improvement of sample intercritically step quenched at 770°C and tempered at 320°C for 1 h (G770T) with some selected samples (A, G750 and G770).

Property	Sample				% Improvement of G770T Over		
	A	G750	G770	G770T	A	G770	G750
Hardness (Hv)	161.7	345.1	241.45	327.15	102.32	35.49	-5.20
I.S. (J/mm ²)	1.30	0.18	0.26	1.66	27.69	538.46	822.22
TEL (%)	21.97	15.43	9.14	36.03	64.0	294.20	133.51
UTS (N/mm ²)	670.55	1184.64	785.68	1569.28	134.03	99.74	32.47

slow (furnace) cooling of austenite from 850°C to intercritical annealing temperatures of 790, 770, 750 and 730°C, took 7, 10, 14, and 19 min respectively, resulting in the formation of pro-eutectoid ferrite (light areas) and austenite, which transformed to large martensite laths (grey areas) on quenching from the intercritical temperature region (Figure 5(a) and (c)) respectively. Smallman stated that the morphology of this ferrite depends on the usual precipitation variables such as temperature, time, carbon content and grain size, and that growth occurs preferentially at grain boundaries and on certain crystallization Figures (Smallman, 1995). Honeycombe and partner further postulated that grain boundary allotriomorphs are the first morphology of ferrite to appear over the whole range of composition and temperature (Honeycombe and Bhadeshia, 1995). These they claim to predominate above 800°C, and grow along the grain boundaries and also into the austenite grains to give a well-defined grain structure. These features are clearly revealed in Figure 5(b). Precipitation of carbide particles is also noticed along the grain boundaries as temperature is increased, (Figure 5(b) and (c)). These carbide particles pin down the ferrite grains at locations where they are precipitated and therefore hinder the rather regular growth of the ferrite along the grain boundaries. The result of this, as seen in Figure 5(c) and (e), is that the ferrite grains are of irregular shapes mixed with equally irregularly curved globular martensite constituting a continuous network along prior austenite grain boundaries.

Figure 5(a) reveals irregularly shaped recrystallized ferrite (bright) and lath martensite (gray) precipitated along prior austenite grain boundaries in a net work of ferrite (light) with little retained austenite (dark). Figure 5(b) also reveals nucleated ferrite (bright) precipitated along prior austenite grain boundaries, tempered martensite (gray) in a ferrite (light) matrix, with dispersion of fine carbide (dark) precipitated from tempered martensite and retained austenite. More irregularly shaped ferrite (bright) and lath martensite (gray) precipitated along prior austenite grain boundaries in a network of ferrite (light) was observed in Figure 5(c) with very little retained austenite (dark). In Figure 5(d), fine grained tempered martensite (gray) in a network of ferrite (light) with dispersion of fine carbide (dark) precipitated

from tempered martensite and retained austenite was observed. Figure 5(e) reveals lath martensite (gray) and recrystallized ferrite (bright) along prior austenite grain boundaries in a net work of ferrite (light) with some retained austenite (dark). Also, in Figure 5(f) fine grained tempered martensite (gray) in a net work of ferrite (light) matrix with dispersion of carbide (dark) precipitated from tempered martensite and retained austenite was observed.

Effect of tempering on the properties of step quenched samples

All the accessed properties improved upon tempering (Figures 1 to 4 and Table 4). High strength and ductility observed with the tempered samples could be attributed to factors such as: grain refinement on tempering (Figure 5(c), (d) and (e), (f)) and recrystallization of ferrite from martensite on tempering at 320°C, because at higher intercritical annealing temperatures of the step quench process there are numerous prior austenite grain boundaries present which favour nucleation and recrystallization of ferrite on tempering than at lower temperatures. This enhances the synergy between plasticity and elasticity of martensite and ferrite respectively during deformation.

For hardness, after tempering for 1 h at 320°C, a minimum value was reached at 750°C (Figure 2). The decrease in hardness could be attributed to softening effect of the hard martensite and recrystallization of more ferrite on tempering. While the increased hardness of the G770T over G770 could be as a result of refinement of the coarse grains on tempering (Figure 5(e) and (f)). Table 4 shows that all the properties have positive improvement after tempering. Hardness value improved by 102.32% over the normalized sample while it improved by 35.49% over the intercritically step quenched sample. The high level of improvement observed could be attributed to the redistribution of carbon on tempering. Grain refinement on tempering the sample step quenched at 770°C could also account for the improvement of properties observed (Figure 5(f)). The high improvement observed for impact strength and ductility (TEL) will make this particular sample, G770T

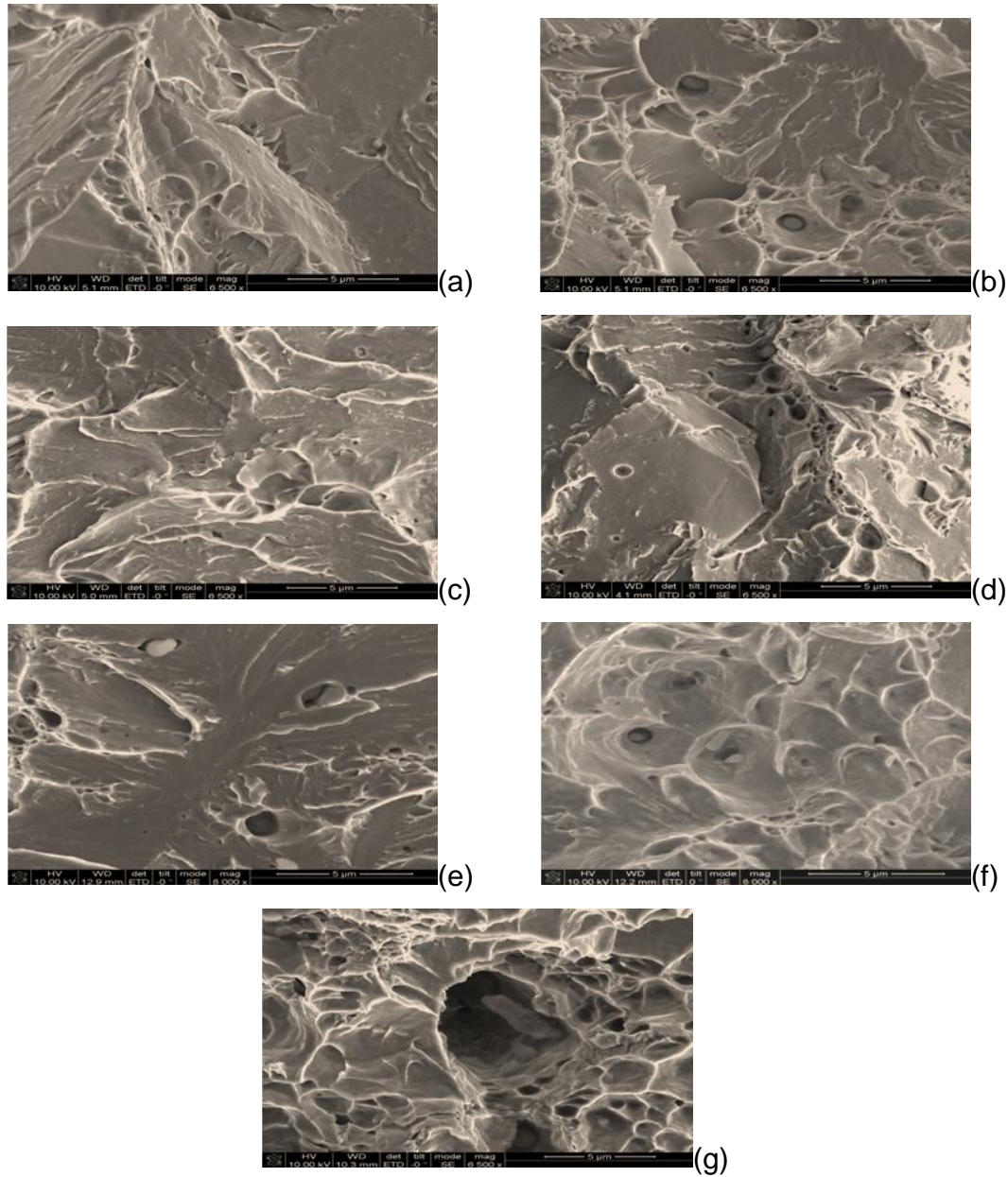


Figure 6. (a) SEM of G730: cleavage ridge-like surface is revealed. (b) SEM of G730T: fractured surface is blocky with dendrites crack lines at the crack tips. (The presence of precipitated carbides hinders the movement of dislocations). (c) SEM of G770: Structure reveals large blocky pure cleavage fracture with crack propagation along the grain boundaries. (d) SEM of G770T: structure reveals mixture of fibrous and cleavage fracture surface with more of the fibrous features at the centre. (e) SEM of G750T: structure reveals mixture of cleavage and fibrous surface. (f) SEM of G750: structure reveals almost pure cleavage fractured surface. (g) SEM of A: structure reveals mixture of fibrous and cleavage surfaces.

unique in terms of formability or workability and ability to withstand both high static and sudden loading.

Effects of process parameters on the fractography

Figure 6 shows the scanning electron micrographs of the fractured surfaces of some developed dual phase

samples after subjecting it to impact test. Figure 6(a) and (b) revealed pure cleavage fracture for G730 and G770 respectively, while Figure 6(c) and (d) revealed a blocky fractured surface with dendrites crack lines at the crack tips and the presence of precipitated carbides for G730T. A mixture of fibrous and cleavage fracture surface with more of the fibrous at the centre for G770T was observed in Figure 6(e). All of this could account for the tremendous

improvement in impact strength observed after tempering of the steels. This phenomenon could be attributed to the dispersion of hard martensite in soft and ductile ferrite matrix naturally exhibited by conventional dual phase steel. Figure 6(g) shows the fractured surface of the normalized sample with mixture of fibrous and cleavage surfaces. A predominantly cup and cone structure was exhibited by the normalized sample thus indicating its failure to be ductile. This justifies the relatively increased strain-to-fracture (TEL) observed (as earlier discussed). Generally, sample G770T was found to develop a unique higher mechanical properties (impact, hardness, tensile strength) with a surprising improvement in the ductility. These exhibited properties make it suitable for structural applications.

Conclusion

From the foregoing, it can be concluded that tempering intercritically step quenched 0.234wt%C steel at 320°C improved all the investigated properties, both on the normalized and as-step quenched steels. The tremendous improvement recorded for UTS, TEL and IS will make the tempered steel put up outstanding performance in the automotive industry where high strength, light weight and ability to maintain high crash safety are required. Also, a combination of high hardness, high UTS and good toughness will promote its application in the oil and gas sector for the construction of pipelines used for conveying high pressured petroleum products and crude. It will also perform maximally in structural designs such as sky scrapers, bridges, towers etc. Hence, these steels are strongly recommended for use in the above mentioned industries.

Conflict of Interest

The authors have not declared any conflict of interest.

REFERENCES

- Alaneme KK, Ranganathan S, Mojisola T (2010). Mechanical Behaviour of Duplex Phase Structures in a Medium Carbon Low Alloy Steel. *J. Minerals Mater. Charact. Eng.* 9(7):621–633. DOI: 10.4236/jmmce.2010.97044.
- ASTM E8M-91 (1992). Standard Test Method for Tension Testing of Metallic Materials [Metric]. In: Annual Book of ASTM Standards: ASTM International. P. 160.
- Bag A, Ray K, Dwarakadasa ES (1999). Influence of Martensite Content and Morphology of Tensile and Impact Properties of High-Martensite dual-phase steels. *Metall. Mater. Trans A.* 30A. P. 1193.
- Bello KA, Hassan SB, Abdulwahab M (2007). Effects of Tempering on the Microstructures and Mechanical Properties of Low Carbon, Low Alloy Martensitic Steel. *J. Appl. Sci. Res.* 3(12):1719–1723.
- Daramola OO, Adewuyi BO, Oladele IO (2010). Effects of Heat Treatment on the Mechanical Properties of Rolled Medium Carbon Steel. *J. Minerals Mater. Charact. Eng.* 9(8):693–708. DOI: 10.4236/jmmce.2010.98050.
- Honeycombe RWK, Bhadeshia HKDH (1995). *Steels, Microstructure and properties* 2nd Ed., Edward Arnold, London.
- Majid P (2010). Tensile Strength and Ductility of Ferrite – Martensite Dual Phase Steels. *Assoc. Metallurgical Engineers Serbia (AMES)*. pp. 187–194.
- Mohammad RA, Ekarami A (2008). Effect of Ferrite Volume Fraction on Work Hardening Behaviour of High Bainite Dual Phase (DP) Steels [J]. *Mater. Sci. Eng. A.* 477:306-310.
- Offor PO, Ezekoye VA, Ezekoye BA (2010). Influence of Heat Treatment on the Mechanical Properties of 0.13Wt% Structural Steel. *Pacific J. Sci. Technol.* 11(2):16–21.
- Sang YK, Jin WP, Jung DL (2006). Application of high strength steel in a new automotive crankshaft. *New Developments Products Proceedings*. P. 3.
- Smallman RE (1995). *Modern physical Metallurgy*, 9th ed., Butterworth Heinemann Ltd, Oxford.
- Yazici M, Durmus A, Bayram A (2009). Influence of Morphology of Martensite on Tensile and Strain Hardening Properties of Dual Phase Steels. *Materalprufung* 45(5):214–219.
- Zhao ZZ, Jin GC, Niu F, Tang D, Zhao AM (2009). Microstructure Evolution and Mechanical Properties of 1000MPa Cold Rolled Dual-Phase Steel. *Transactions of Nonferrous Metals Society of China*, Elsevier Science Press 19:S563–S568.

Full Length Research Paper

Existence of solution for a third order three point boundary value problem at resonance

S. A. Iyase and M. C. Agarana*

Department of Mathematics, Covenant University, P. M. B. 1023, Ota, Ogun State, Nigeria.

Received 17 June 2015; Accepted 4 August, 2015

Using coincidence degree arguments we prove some existence results, for a third order three point boundary value problem at resonance.

Key words: Resonance, coincidence degree, third order, three point boundary value problem.

INTRODUCTION

In this paper, we shall discuss the solvability of the three point boundary value problem of the form

$$x'''(t) = f(t, x, x', x'') \quad (1)$$

$$x'(1) = x''(0) = 0, x(1) = ax(\eta) \quad (2)$$

Where $a = 1$ and $f: [0,1] \times \mathbb{R}^3 \rightarrow \mathbb{R}$ is continuous and $\eta \in (0,1)$.

Multipoint boundary value problems arise in a variety of different areas of Applied Mathematics, Physics and Engineering. For example, in solving partial differential equations by the method of separation of variables, one comes across differential equations whose solutions must satisfy boundary conditions at several points. Similarly bridges of various sizes are sometimes contrived with multipoint supports which correspond to a multipoint boundary condition. Boundary value Problem (1) to (2) is called a problem at resonance if $Lx = x'''(t) = 0$ has non-trivial solutions under the boundary Conditions (2)

that is, when $\dim \ker L \geq 1$. On the interval $[0,1]$ second order and third order multipoint boundary value problems have been studied by Aftabizadeh et al. (1989); Constantin (1996); Feng and Webb (2001); Gregus et al. (1971); Gupta and Lakshmikantham (1991); Gupta et al. (1995); Liu and Yu (1995) and Ma (1997, 1998). Our method of proof consists of imposing a decomposition condition on f of the form

$$f(t, x, y) = g(t, x, y) + h(t, x, y) \quad (3)$$

We shall then employ coincidence degree arguments to obtain our existence results. In what follows, we shall use the norm $\|x\|_\infty = \max_{t \in [0,1]} |x(t)|$. We denote the norm in $L^1[0,1]$ by $\|\cdot\|_1$ and on $L^2[0,1]$ by $\|\cdot\|_2$.

Examples are the vibrations of a guy wire of a uniform cross composed of N parts of different densities (Moshiasky, 1981) and some problems in the theory of elastic stability (Timoshenko, 1961).

*Corresponding author. E-mail: michael.agarana@covenantuniversity.edu.ng

PRELIMINARIES

Consider the linear equation

$$Lx = x'''(t) = 0 \tag{4}$$

$$x'(1) = x''(0) = 0, x(1) = ax(\eta) \tag{5}$$

If we assume a solution of the form

$$x(t) = \sum_{i=0}^3 a_i t^i$$

Then this solution exists if and only if

$$a_3(1 - a) = 0 \tag{6}$$

The case where $a \neq 1$ which corresponds to the non-resonance case was discussed in Iyase (2005)

When $a = 1$, Equations (4) to (5) has non-trivial solutions. Therefore, problem (1) to (2) is at resonance. We shall prove existence results for the boundary value problem (1) to (2) under the Condition (6) when $a = 1$.

In our proof we shall need the following Continuation Theorem based on Mawhin's coincidence degree.

Theorem 1

Mawhin (1979) Let L be a Fred Holm operator of index zero and let N be L -compact on $\overline{\Omega}$. Assume that the following conditions are satisfied:

- (1) $Lx \neq Nx$ for any $(x, \lambda) \in (\text{dom } L \cap \partial\Omega) \times (0, 1)$
- (2) $QNx \neq 0$ for $x \in \ker L \cap \partial\Omega$
- (3) The Brower degree $\text{deg}_B((JQN)_{\ker}, \Omega \cap \ker L, 0) \neq 0$

Where $J : \text{Im } Q \rightarrow \ker L$ is some isomorphism.

Then there exists $x \in \overline{\Omega} \cap \text{dom } L$ such that

$$Lx = Nx \tag{7}$$

Let $X = C^2[0, 1]$, $Z = L^1[0, 1]$

Let $L : \text{dom } L \subset X \rightarrow Z$ be defined by

$$Lx = x'''(t) \tag{8}$$

Where

$$\text{dom } L = \{x \in W^{3,1}(0, 1), x'(1) = x''(0) = 0, x(1) = x(\eta)\}.$$

We define $N : X \rightarrow Z$ by setting

$$Nx = f(t, x(t), x'(t), x''(t)) \tag{9}$$

Then the boundary value Problem (1) to (2) can be put in the form

$$Lx = Nx \tag{10}$$

Lemma 1

If L and N are defined as in Equations (8) and (9), then

$$\text{Im } L = \left\{ y \in Z : \int_{\eta}^1 \int_t^1 \int_0^r y(s) ds dr dt = 0 \right\}$$

$L : \text{dom } L \subset X \rightarrow Z$ is a Fred Holm operator of index zero.

Proof

We will show that the problem

$$x'''(t) = y \text{ for } y \in Z \tag{11}$$

has a solution $x(t)$ satisfying

$$x'(1) = x''(0) = 0, x(1) = x(\eta) \tag{12}$$

If and only if

$$\int_{\eta}^1 \int_t^1 \int_0^r y(s) ds dr dt = 0 \tag{13}$$

Suppose Equation (11) has a solution $x(t)$ satisfying Equation (12) then from Equation (11) we have

$$0 = \int_{\eta}^1 \int_t^1 \int_0^r x'''(s) ds dr dt = \int_{\eta}^1 \int_t^1 \int_0^r y(s) ds dr dt$$

Now suppose $\int_{\eta}^1 \int_t^1 \int_0^r y(v) dv dr dt = 0$.

Let

$$x(t) = c - \frac{t}{1-\eta} \int_{\eta}^1 \int_0^r \int_0^w y(v) dv dw dr + \int_0^t \int_0^r \int_0^w y(v) dv dw dr \tag{14}$$

Then $x(t)$ is a solution of Equation (11) with

$$\int_{\eta}^1 \int_t^1 \int_0^r y(s) ds dr dt = 0.$$

For $y \in Z$ we define the projection $Q : Z \rightarrow Z$ by

$$Qy = \frac{6}{(\eta + 2)(\eta - 1)^2} \int_{\eta}^1 \int_t^1 \int_0^r y(s) ds dr dt, y \in Z \tag{15}$$

Let $y_1 = y - Qy$, that is $y_1 \in \ker Q$. Then by direct calculations we have

$$\int_{\eta}^1 \int_t^r y_1(v) dv dr dt = \int_{\eta}^1 \int_t^r y(v) dv dr dt \left[1 - \frac{6}{(\eta+2)(\eta-1)^2} \int_{\eta}^1 \int_t^r dv dr dt \right] = 0$$

So $y_1 \in \text{Im } L$. Hence $Z = \text{Im } L + \text{Im } Q$.

Since $\text{Im } L \cap \text{Im } Q = \{0\}$ we obtain

$$Z = \text{Im } L \oplus \text{Im } Q$$

Now $\ker L = \{x \in \text{dom } L : x = c, c \in \mathbb{R}\}$.

Hence $\dim \ker L = \dim \text{Im } Q = 1$.

Therefore, L is a Fredholm operator of index zero.

Let $P : X \rightarrow X$ be defined by

$$Px(t) = x(0), t \in [0, 1]$$

Let

$$L_p = L|_{\text{dom } L \cap \ker P} \tag{16}$$

The operator $K = L_p^{-1} : \text{Im } L \rightarrow \text{dom } L \cap \ker P$ is the linear operator defined by

$$(Ky)(t) = \frac{1}{2} \int_0^t (t-s)^2 y(s) ds$$

By the Azela-Ascoli Theorem it can be shown that K is compact. Hence N is L -compact. We recall that a linear mapping

$$L : \text{Dom } L \subset X \rightarrow Z$$

With

$$\ker L = L^{-1}(0)$$

And

$$\text{Im } L = L(\text{Dom } L)$$

Will be called a Fredholm mapping if the following two conditions hold:

- (i) $\ker L$ has a finite dimension
- (ii) $\text{Im } L$ is closed and has a finite codimension

We also recall that the codimension of $\text{Im } L$ is the dimension of $Z/\text{Im } L$ that is, the dimension of the cokernel of L . When L is a Fredholm mapping, its Fredholm index is the integer.

$$\text{Ind } L = \dim \text{Ker } L - \text{Codim } \text{Im } L$$

We say that a mapping N is L -compact on Ω if the mapping $QN : \bar{\Omega} \rightarrow Z$ is continuous, $QN(\bar{\Omega})$ is bounded, and $Kp(I-Q)N : \bar{\Omega} \rightarrow X$ is compact, that is, it is continuous and $Kp(I-Q)N(\bar{\Omega})$ is relatively compact, where $Kp : \text{Im } L \rightarrow \text{Dom } L \cap \text{Ker } P$ is the inverse of restriction L_p to $\text{Dom } L \cap \text{Ker } P$, so that $LKp = I$ and $KpL = I - P$.

MAIN RESULTS

Theorem 2

Assume that $f : [0, 1] \times \mathbb{R}^3 \rightarrow \mathbb{R}$ is continuous and has the decomposition

$$f(t, x, y, z) = g(t, x, y, z) + h(t, x, y, z) \tag{17}$$

such that

- (i) $xf(t, x, y, z) > 0$ for a.e $t \in [0, 1]$ and $(x, y, z) \in \mathbb{R}^3$
- (ii) $yg(t, x, y, z) \geq 0$
- (iii) $|h(t, x, y, z)| \leq M \{ |x| + |y| + |z|^\beta \}$ for $0 \leq \beta < 1$
- (iv) $zf(t, x, y, z) \leq (|z|^2 + 1)(D(t, x, y, z) + \alpha(t))$

Where $D(t, x, y, z)$ is bounded on bounded sets and $\alpha \in L^1[0, 1]$

Then the boundary value Problem (1) to (2) has at least one solution in $C^2[0, 1]$ provided

$$M < \frac{\pi^3}{16\sqrt{4 + \pi^2}} \tag{18}$$

Proof

Let L be defined as in Equation (8). Then $\ker L = \{x \in X : x \text{ is a constant mapping}\} = \mathbb{R}$.

We shall prove that the conditions of Theorem 1 are satisfied. To do this, we shall show that for $\lambda \in (0, 1)$ the set of solutions of the family of equations

$$x'''(t) = \lambda f(t, x, x', x'') \tag{19}$$

$$x'(1) = x''(0) = 0, x(1) = x(\eta) \tag{20}$$

is a priori bounded and then construct Ω accordingly.

Let $x \in C^2 [0,1]$ satisfy Equation (19) to (20). Since $x(1) = x(\eta)$ there exists $\zeta \in (\eta,1)$ such that $x'(\zeta) = 0$ and from $x'(1) = x'(\zeta) = 0$ there exists $t_1 \in (\zeta,1)$ such that $x''(t_1) = 0$. Hence from condition (i) of Theorem 2 we derive that if $x(t) > 0$ then

$$0 = \int_0^1 x'''(s) ds = \lambda \int_0^1 f(s, x(s), x'(s), x''(s)) ds > 0$$

Which is a contradiction. If $x(t) < 0$ we derive a similar contradiction. Hence there exists $t_0 \in (0,t_1)$ such that $x(t_0) = 0$. Therefore for each $t \in [0,1]$ we have

$$|x|_2^2 \leq \frac{4}{\pi^2} |x'|_2^2 \tag{21}$$

Multiplying Equation (19) by $x'(t)$ and using the relation $x'(1) = x''(0) = 0$

yields

$$\int_0^1 x'(t)x'''(t) dt = -\int_0^1 |x''|^2 dt .$$

Hence

$$\int_0^1 |x''|^2 dt = -\lambda \int_0^1 x'(t)g(t, x, x', x'') dt - \lambda \int_0^1 x'(t)h(t, x, x', x'') dt$$

Using the Cauchy inequality

$$|ab| \leq \frac{\epsilon a^2}{2} + \frac{b^2}{2\epsilon} \text{ for } \epsilon > 0$$

we have

$$\int_0^1 |x'(t)||h(t, x, x', x'')| dt \leq \frac{\epsilon}{2} \int_0^1 |x'|^2 dt + \frac{1}{2\epsilon} \int_0^1 |h(t, x, x', x'')|^2 dt$$

From condition (iii) we obtain the estimate

$$|h(t, x, y, z)|^2 \leq 4M^2 \left\{ |x|^2 + |y|^2 + |z|^{2\beta} \right\}$$

Therefore from Holder's inequality we get

$$|x''|_2^2 - \frac{\epsilon}{2} |x'|_2^2 \leq \frac{2M^2}{\epsilon} \left\{ |x|_2^2 + |x'|_2^2 + |x''|_2^{2\beta} \right\}$$

since $x'(1) = 0$ we obtain

$$\frac{1}{2} |x''|_2^2 + \left(\frac{\pi^2}{8} - \frac{\epsilon}{2} \right) |x'|_2^2 \leq \frac{2M^2}{\epsilon} \left\{ |x|_2^2 + |x'|_2^2 + |x''|_2^{2\beta} \right\} \tag{22}$$

Using Equation (21) in (22) we get

$$\frac{1}{2} |x''|_2^2 + \left(\frac{\pi^2}{8} - \frac{\epsilon}{2} - \frac{8M^2}{\epsilon\pi^2} - \frac{2M^2}{\epsilon} \right) |x'|_2^2 \leq \frac{2M}{\epsilon} |x''|_2^{2\beta} \tag{23}$$

Since $0 \leq \beta < 1$ we infer the existence of a constant M_1 such that

$$|x'|_2 < |x''|_2 < M_1 \tag{24}$$

Provided

$$\frac{\pi^4}{8} > \frac{8M^2}{\epsilon} + \frac{2\pi^2 M^2}{\epsilon} + \frac{\epsilon\pi^2}{2} \tag{25}$$

The choice $\epsilon = 2M\sqrt{4 + \pi^2}$ minimizes the right hand side of Equation (25) and the minimum value is $2M\pi\sqrt{4 + \pi^2}$. Therefore Equation (25) holds provided

$$M < \frac{\pi^3}{16\sqrt{4 + \pi^2}} \tag{26}$$

Furthermore, since $x(t_0) = x'(1) = 0$ for $t_0 \in (\eta,1)$, we get from Equation (24) that

$$|x|_\infty < |x'|_\infty < M_2, \quad M_2 > 0 \tag{27}$$

From condition (iv) of Theorem 2 we obtain

$$\frac{x''x'''}{|x''|^2 + 1} \leq D(t, x, x') + \alpha(t) \tag{28}$$

Integrating Equation (28) from 0 to t we get

$$\log_e |x''| \leq \int_0^t \frac{x''(s)x'''(s)}{|x''(s)|^2 + 1} ds = \left[\frac{1}{2} \log_e (|x''(s)|^2 + 1) \right]_0^t < D + |\alpha|_1 = N_0 \tag{29}$$

Where the constant D depends only on M_2 . Furthermore since $x''(0) = 0$ we get from Equation (29) that

$$|x''|_{\infty} < e^{N_0} = M_3 \tag{30}$$

Let

$$\|x\| = \max(|x|_{\infty}, |x'|_{\infty}, |x''|_{\infty}) < \max(M_2, M_3) = A$$

It follows that $\|x\| < A$.

We take $\Omega = \{x \in X : \|x\| < A\}$ then if $x \in \text{dom } L \cap \partial\Omega$ then $Lx \neq \lambda Nx, 0 < \lambda < 1$.

If $x \in \ker L \cap \partial\Omega$ then $x = \pm A$.

Now if $x = A$ we derive from condition (i) of Theorem 2 that $QNx = \frac{6}{(\eta+2)(\eta-1)^2} \int_{\eta}^1 \int_t^1 \int_0^r f(s, A, 0, 0) ds dr dt > 0$

and if $x = -A$ we get $QNx < 0$

Thus $QNx \neq 0$ for $x \in \ker L \cap \partial\Omega$.

Verifying Condition (2) of Theorem 1

It is easily verified that

$$H(\mu, x) = \mu x + (1 - \mu)QNx, 0 \leq \mu < 1$$

is a homotopy from the identity I to QN on $\bar{\Omega}$ and is such that $H(\mu, x) \neq 0$ on $[0, 1] \times (\partial\Omega \cap \ker L)$

Hence taking J in Condition (3) of Theorem 1 to be the identity we get

$$\text{deg}_{\beta} [QN|_{\ker L}, \Omega \cap \ker L, 0] = \text{deg}_{\beta} [I, \Omega \cap \ker L, 0] = 1$$

This completes the proof of Theorem 2.

Remark 1

The results of Theorem 2 still hold if condition (i) is replaced by

$$xf(t, x, y, z) < 0.$$

Remark 2

The results of Theorem 2 remain valid if assumption (i) is replaced by any of the following assumptions:

$$(1) |h(t, x, y, z)| \leq M(|x| + |y|^{\beta} + |z|) \text{ for } 0 \leq \beta < 1$$

provided $M < \frac{\pi}{8\sqrt{16 + \pi^4}}$

$$(2) |h(t, x, y, z)| \leq M(|x|^{\beta} + |y| + |z|) \text{ for } 0 \leq \beta < 1$$

provided $M < \frac{1}{\pi}$

$$(3) |h(t, x, y, z)| \leq M(|x|^r + |y|^{\beta} + |z|^p) \text{ for } 0 \leq \beta, r, p < 1$$

for some constant M .

CONCLUSION

In this paper, by using a continuation theorem based on coincidence degree theory, we obtained the existence of solution for a third order boundary value problem at resonance. For the research on the existence of solution of linear and non-linear boundary value problem. Coincidence degree theory plays an important role.

Conflict of Interest

The authors have not declared any conflict of interest.

REFERENCES

Aftabizadeh AR, Gupta CP, Jian MX (1989). Existence and Uniqueness Theorems for three point boundary value problems. *SIAM. J. Math. Anal.* 20:716-726.

Constantin A (1996). A note on a boundary value problem. *Nonlinear Anal.* 27(1):13-16.

Feng W, Webb JRL (2001). Solvability of three point boundary value problems at resonance. *Nonlinear Anal. Theory methods. Appl.* 47:2407-2418.

Gregus RE, Neumann F, Arscott M (1971). Three point boundary value problem for differential equations. *J. London Math. Soc.* 3:429-436.

Gupta CP, Lakshmikantham V (1991). Existence and uniqueness theorems for a third order three point boundary value problem. *Nonlinear Anal.* 16:949-957.

Gupta CP, Ntouyas K, Tsamatos P (1995). Solvability of an m-point boundary value problem for second order ordinary differential equations. *J. Math. Anal Appl.* 189:575-584.

Iyase SA (2005). Existence Theorems for a third order three point boundary value problem. *J. Nig. Math. Soc.* 24:17-23.

Liu B, Yu S (1995). Solvability of multipoint boundary value problem set resonance (III). *Appl. Math. Comput.* 129:1483-1489.


Ma RY (1997). Existence Theorem for a second order three point boundary value problem. *J. Math. Anal. Appl.* 212:430-442.

Ma RY (1998). Multiplicity results for a third order boundary value problem at resonance. *Non Linear Anal. Theory Methods. Appl.* 32:493-499.

Mawhin J (1979). *Topological degree Methods in Non-Linear boundary value problems.* NSF. BMS Reg.Conf. Ser. Math 40. Americ. Math. Soc. Providence R.I.

Moshiasky M (1981). Sobre Los prolemas de condiciones a La frontiers en una dimension de caracteristicas discontinues. *BoL soc. Mat Mexicana* 7.

Timoshenko S (1961). *Theory of Elastic Stability.* McGraw-Hill. NewYork 1961.



International Journal of Physical Sciences

Related Journals Published by Academic Journals

- *African Journal of Pure and Applied Chemistry*
- *Journal of Internet and Information Systems*
- *Journal of Geology and Mining Research*
- *Journal of Oceanography and Marine Science*
- *Journal of Environmental Chemistry and Ecotoxicology*
- *Journal of Petroleum Technology and Alternative Fuels*

academicJournals